## TITLE

# Membrane phase separation drives organization at B cell receptor clusters

## AUTHORS/AFFILIATIONS

Sarah A. Shelby[1], Ivan Castello-Serrano[2], Kathleen C. Wisser[1], Ilya Levental[2], and Sarah L. Veatch[1]*

[1] Program in Biophysics, University of Michigan, Ann Arbor, MI 48109 USA

[2] Department of Molecular Physiology and Biological Physics, University of Virginia, Charlottesville, VA 22903 USA

## AUTHOR LIST FOOTNOTES

*Correspondence: sveatch@umich.edu

## SUMMARY

Isolated plasma membranes separate into two coexisting liquid phases with distinct lipid and protein compositions but live cell plasma membranes do not macroscopically phase separate, leading to questions of whether and how the membrane phase transition contributes to functional heterogeneity in cells. Using quantitative super resolution microscopy we show that B cell receptor signaling platforms are nanoscale domains that quantitatively enrich membrane probes based on probe phase partitioning in isolated plasma membrane vesicles. Phase partitioning in vesicles also predicts relative probe mobility and retention at receptor clusters. The convergence between measurements in live cells and isolated membranes establishes a clear role for the membrane phase transition as an organizing principle in cells. We propose that physical properties fundamental to the membrane phase transition give rise to a plasma membrane that is a highly responsive medium, capable of compartmentalizing cellular processes in response to diverse stimuli.

## KEYWORDS

phase separation, lipid rafts, immune receptor signaling, liquid-ordered phase, liquid-disordered phase, single molecule fluorescence localization microscopy, plasma membrane.

## INTRODUCTION

The impact of phase separation within cells has become appreciated in recent years, largely through visualizations of micron-scale, high-contrast protein- and/or RNA-rich liquid droplets in the cytoplasm and nucleus (Lyon et al., 2021; Shin and Brangwynne, 2017). Analogous phase separation has long been proposed to be an organizing principle in cell membranes, especially within the plasma membrane, where domains are often referred to as “lipid rafts” (Simons and Ikonen, 1997). Despite decades of research, direct evidence for phase separation within the intact plasma membrane has proven elusive, and the simplistic models used to rationalize rafts either lack utility or are easily disproved, leading to valid skepticism (Kenworthy, 2008; Munro, 2003). Recent years have brought several promising measurements using methods sensitive to single molecule dynamics, molecular-scale organization, or membrane material properties (Eggeling et al., 2009; Koyama-Honda et al., 2020; Sanchez et al., 2012; Sengupta et al., 2007), though directly relating these observations to principles of membrane phase separation has proven difficult. In contrast, plasma membranes isolated from cells can clearly separate into coexisting liquid-ordered (Lo) and liquid-disordered (Ld) phases (Baumgart et

al., 2007), and there is clear evidence that membrane composition is carefully tuned to support a wide variety of biological functions (Ernst et al., 2016; Lingwood and Simons, 2010).

An increasingly sophisticated picture of the thermodynamics of phase separation in membranes provides insight into how phase separation could manifest as heterogeneity in the intact plasma membrane and how such features could be accessed experimentally (Levental et al., 2020a; Shaw et al., 2021). Specifically, several proposed physical models explain how mechanisms rooted in phase separation lead to structure in membranes consistent with rafts as small and dynamic membrane domains or larger domains scaffolded by membrane proteins (Schmid, 2017). Some models show that membranes without macroscopic phase separated domains can still retain some properties of phase separated systems, raising the possibility of a connection between phase separation, "lipid rafts", and the impact of membrane composition on biological function.

Here, we test if concepts of phase separation translate to intact cell membranes using single molecule fluorescence localization microscopy in living B cells. Since the thermodynamics of phase separation dictates the composition of coexisting phases, we directly measure the concentration of probe molecules at high spatial resolution. Our methods are sensitive and quantitative, and exploit the signaling platforms that assemble following B cell receptor (BCR) activation to template long lived membrane domains (Gold and Reth, 2019; Gupta and DeFranco, 2007; Pierce and Liu, 2010; Sohn et al., 2006; Stone et al., 2017). Because plasma membrane components experience a combination of strong, protein-mediated and weaker-but-collective, membrane-mediated interactions, we interrogate numerous membrane probes spanning many classes of components to isolate a generic contribution from phase separation. With this extensive dataset, we quantify the extent to which local concentration and dynamics depend on probe phase preference measured by their partitioning in phase separated plasma membrane vesicles. We demonstrate that anchor phase preference is a quantitative determinant of its local concentration and dynamics within BCR signaling platforms. This convergence between live cell and equilibrated vesicle measurements directly and conclusively establishes phase separation as an organizing principle in cell plasma membranes.

## RESULTS

### BCR clusters mark stabilized domains in the plasma membranes of B cells.

Figure 1 shows CH27 B cells expressing the fluorophore mEos3.2 anchored to the plasma membrane via similar yet biophysically distinct lipidated peptide motifs. One motif contains myristoyl and palmitoyl groups (PM) and the second contains a myristoyl modification appended to a polybasic sequence (M). Both are derived from Src family kinases that anchor to the inner leaflet of the plasma membrane. These probes are imaged in live cells alongside BCR labeled with an antibody fragment (Fab) against the μ subunit of IgM BCR that is both biotinylated and fluorescently tagged with an organic fluorophore (silicon rhodamine, SiR). Probes are imaged in cells under conditions where probes are isolated and can be localized, and reconstructed images show the positions of probes acquired over time — in Fig 1A, from 2 to 10 min following BCR crosslinking by streptavidin. BCR crosslinking reorganizes receptors into tight clusters (Pierce and Liu, 2010), producing reconstructed images in which puncta decorate the ventral cell surface while both PM and M anchors are more uniformly distributed over the cell surface. Both single molecules and BCR puncta are dynamic. Supplementary Movies 1-6 show single molecule motions and the evolution of BCR clusters over time.

We have previously developed analytical methods for quantifying co-localization in super-resolved dynamic systems using spatio-temporal cross-correlation (Stone and Veatch, 2015). Cross-correlation functions are histograms of the pairwise distances between localized single molecules observed in different color channels, normalized by the frequency of expected pairs in a randomized co-distribution within the same region of interest. Ideally, such cross-correlation functions would be calculated from pairs of molecules observed simultaneously in each frame, i.e. with separation time ($\tau$) = 0 over a time window ($\Delta t$) equal to the integration time of the measurement ($\Delta t$=20ms). However, such an analysis

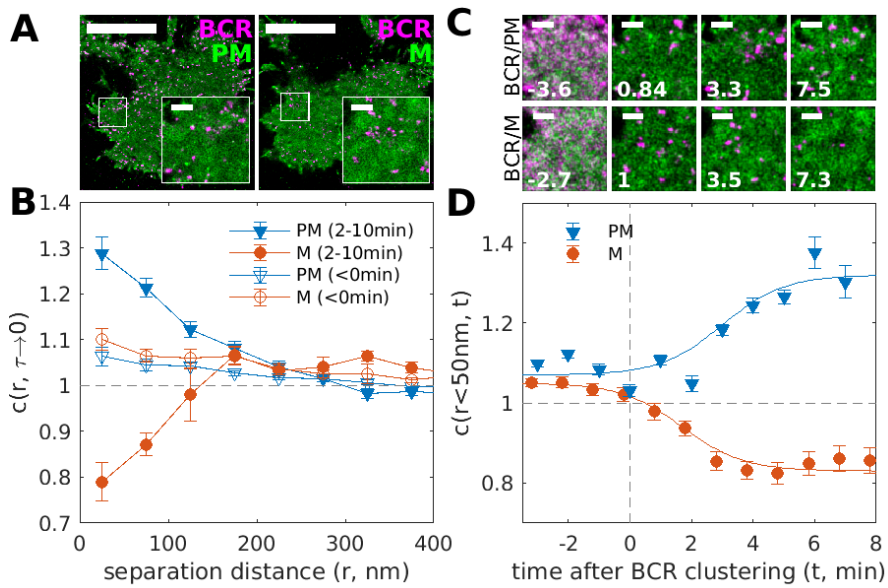


**Figure 1: BCR clustering produces membrane domains that differently sort two fluorescent proteins anchored at the inner leaflet.** (A) Reconstructed live-cell super-resolution images of CH27 B cells imaged between 2 and 10 min after BCR clustering. B cells expressing mEos3.2 conjugated to either a palmitoylated and myristoylated anchor (PM) or a myristoylated anchor (M) (green) are labeled with biotinylated and SiR labeled Fab anti-IgMμ (magenta) that is crosslinked with soluble streptavidin. (B) Quantification of BCR-anchor co-distributions both before (<0min) and after (2-10min) streptavidin addition via the spatial-temporal cross-correlation function c(r, τ) extrapolated to τ=0. Values of $c(r, \tau \to 0) = 1$ indicate a random co-distribution, $c(r, \tau \to 0) > 1$ indicate co-clustering, and $c(r, \tau \to 0) < 1$ indicate exclusion. (C) Images of the region of interest from A reconstructed from 2min of acquired data centered at the time indicated. Time-lapse movies for these cells showing single molecule motions or reconstructed images are included as Supplementary Movies 1-6. (D) The value of the $c(r, \tau \to 0)$ in the first spatial bin (r<50nm) as a function of stimulation time averaged over 5 cells each expressing either PM or M. Cross-correlation amplitudes are evaluated using 2min of acquired localizations centered at the time indicated, as in C. Lines are drawn to guide the eye and are not a fit to any theory. Scale-bars are 10μm in A and are 1μm in A insets and C.

would be inherently statistically underpowered, since experiments are designed to only detect a few single molecules in any single frame. Instead, we collect distances between probes observed in the same frame (τ=0) from many sequential frames spanning a larger time window (Δt~minutes). To further improve counting statistics, and to correct for artifacts due to cross-talk of fluorescent signals across image channels, we also consider pairs detected between frames with small separation-times (τ<2s) and extrapolate to zero separation times ($\tau \to 0$). Cross-correlation histograms are generated with spatial bins = 50nm, such that the first point in all curves reflects the frequency of pairs with separation distances less than 50nm (r<50nm). See Materials and Methods and Supplementary Figure 1 for methodological details.

Figure 1B shows the cross-correlation function, $c(r, \tau \to 0)$, tabulated from the same data used to generate the reconstructed images of Fig 1A (closed symbols), quantifying the differential partitioning of PM and M probes with respect to clustered BCR. The curve for PM takes on values larger than 1 at short separation distances, then decays to 1 as the separation distance increases. The value of $c(r < 50nm, \tau \to 0) = 1.3$ indicates that the local density of PM within 50 nm of the average BCR is 30% greater than the average density in the membrane overall. The inverse behavior is observed for the M anchor, with BCR cross-correlation smaller than 1 at short separation distances and $c(r < 50nm, \tau \to 0) = 0.8$ indicating that M is 20% depleted within 50nm of the average BCR compared to the membrane overall. Cross-correlation functions tabulated from data acquired prior to crosslinking BCR do not show the same differential partitioning (open symbols). Both PM and M anchors are weakly correlated with uncross-linked BCR.

Figures 1C-D show the results of a similar analysis using a shorter time window Δt to better visualize how anchor organization evolves in time. The images in Fig 1C show insets from the same cells as in Fig 1A, but here images are reconstructed only from localizations acquired within Δt=2min windows. Fig 1D shows how the anchor co-localization with BCR evolves with time, focusing only on cross-correlations at short separations from BCR (r<50nm). Prior to crosslinking, BCR is uniformly distributed and is weakly correlated with both of the two anchors. After streptavidin crosslinking, receptors assemble into tight puncta and differential cross-correlations with mEos3.2-anchored peptides emerge over a timescale of several minutes. These results indicate that BCR clusters mark stable membrane domains

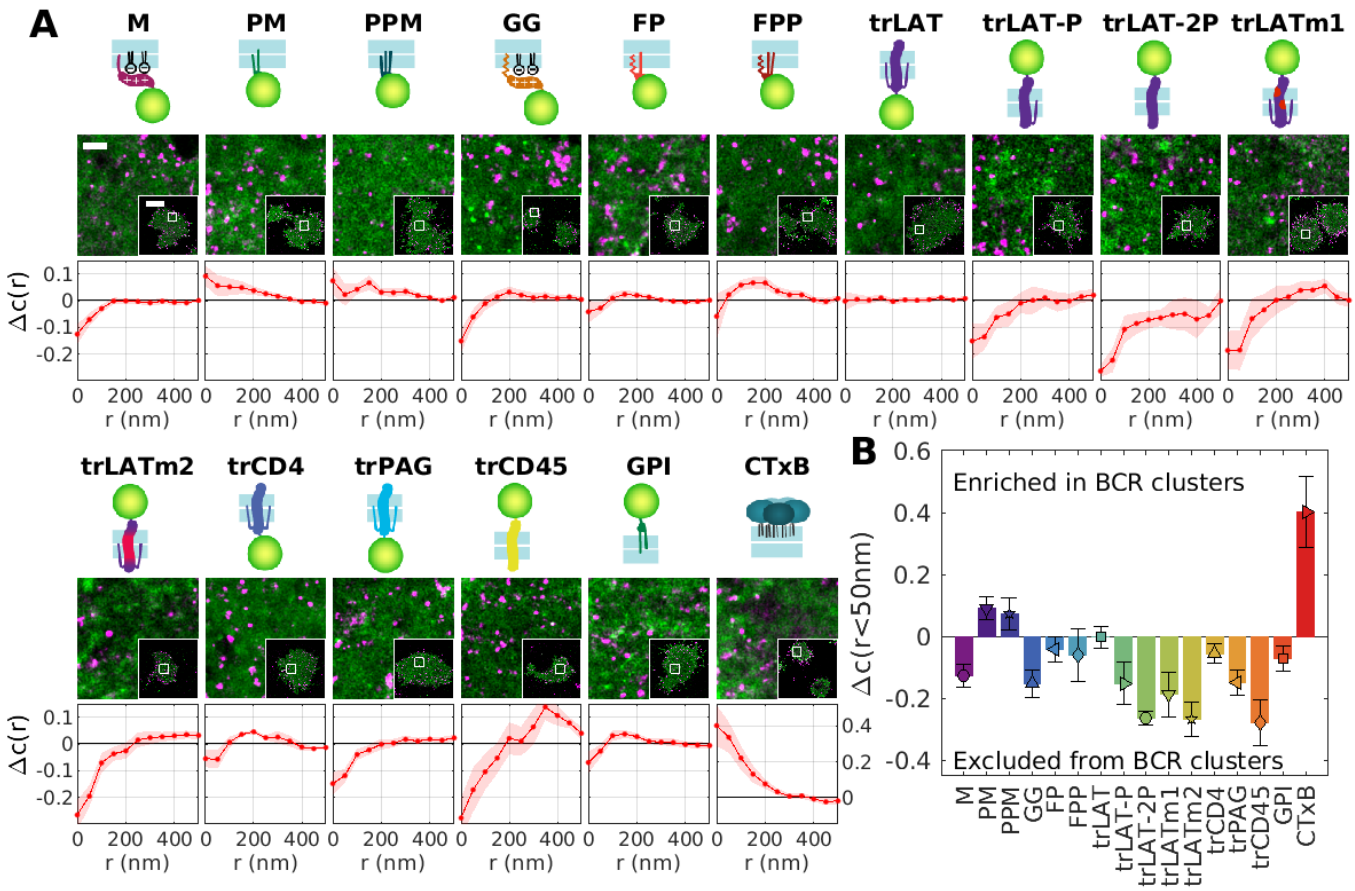


**Figure 2: Anchored probes differentially partition with respect to clustered B cell receptors in live cells.** (A) Schematic representation of anchors used in this study alongside representative reconstructed images showing anchor fluorescence (green) and BCR (magenta). The trace shows the change in c(r) between anchors and BCR for times between 2 and 8 min after BCR clustering and the curve obtained for times before BCR clustering, which we call Δc(r). Error bounds indicated by the shaded region represent the SEM over cells. (B) Summary of Δc(r) for separation distances less than 50nm. Δc(r<50nm) =0 indicates the anchor does not change its co-distribution with respect to BCR when BCR is clustered, Δc(r<50nm) >0 indicates anchors become more enriched near BCR after clustering, and Δc(r<50nm) <0 indicates anchors become more depleted near BCR after clustering.

within the plasma membranes of live B cells that differentially sort probes distinguished only by the structure of their membrane anchors.

**Differential partitioning at BCR clusters extends across a panel of plasma membrane anchors.**

We extended these analyses to a total of 16 plasma membrane probes (presented schematically in Figure 2A; sequences included in Supplementary Table 1) representing different modes of membrane anchorage and expected Lo phase affinities. Many of these probes are truncated anchors from endogenous proteins, while others represent engineered constructs. Representative reconstructed images of these anchors alongside BCR imaged from 2-10 min after BCR crosslinking are shown in Fig 2A, along with curves showing the change in c(r) induced by BCR clustering and cellular activation (Δc(r)). Fig 2B summarizes the magnitude of crosslinking-induced changes in c(r) across all anchors at the smallest separation distances (r<50nm) (see Supplementary Figures 2-3 for raw cross-correlation curves, summary histograms, and distributions of individual cell values).

The first class of probes are peripheral and anchored to the plasma membrane inner leaflet via lipidation, sometimes in combination with a polybasic sequence. In addition to M and PM anchors, this class includes the anchor PPM with a myristoylation and two palmitoylation sites, derived from the Src family kinase member Fyn. We also interrogated

anchors of the Ras family GTPases consisting of a prenyl (geranylgeranyl) group and a polybasic sequence (GG), a farnesyl group and a single palmitoylation (FP), or a farnesyl group and two palmitoylations (FPP). Across this series, both anchors lacking palmitoyl groups (M and GG) become robustly excluded from BCR clusters. The palmitoylated anchors become enriched (PM or PPM) or remain neutrally distributed (FP and FPP) within 50 nm of clustered BCR. The second class of membrane anchors are single-pass transmembrane peptides, many of which are palmitoylated at juxtamembrane cysteines. These include several variants of the transmembrane helix of the type III membrane protein Linker for Activation of T cells (transmembrane LAT; trLAT), where either transmembrane residues or palmitoylation sites were modified to influence Lo phase affinity. Also included are minimal transmembrane anchor sequences of CD4, PAG/CBP, and CD45. trLAT does not change its distribution relative to BCR after clustering, while most other transmembrane anchors become excluded to differing degrees. We also examined two probes that localize exclusively to the outer leaflet of the plasma membrane, including exogenous cholera toxin subunit B (CTxB), which binds to up to 5 GM1 ganglioside lipids on the outer leaflet, and a minimal GPI-linked protein anchor. CTxB is highly enriched at BCR clusters, while GPI is somewhat depleted at short separation distances.

The magnitude and shape of the observed Δc(r) curves are impacted by the finite localization precision of the measurement, which is 25-40nm in each color channel, as well as the finite size of BCR clusters, which are estimated to be close to 35nm in radius (Supplementary Figure S4). Estimates of the effect of these factors on Δc(r) can be obtained through deconvolution (Supplementary Figure S5). Based on this analysis, we estimate that the BCR enrichment values reported in Fig 2B underestimate the local enrichment or depletion of these probes at the center of BCR clusters by at least 30%.

Several anchors produce Δc(r) curves with a local maxima away from r<50nm, suggesting that these anchors are maximally enriched at and beyond the boundaries of BCR clusters after B cell activation. This is observed for both FP and FPP inner leaflet anchors, trCD4 of the transmembrane anchors, and GPI of the extracellular anchors (Supplementary Figure S6). We speculate that this could reflect the asymmetric nature of some anchors that contain individual structural elements that may exhibit preferences for different local environments (e.g. prenylation and palmitoylation for FP and FPP). Another possibility is that the center of BCR clusters may represent a crowded environment and some anchors may be excluded due to steric occlusion (possibly trCD4 and/or GPI).

**Differential partitioning of anchors to the Lo phase in GPMVs**

The anchors described in Fig 2 were chosen because they exhibit diverse partitioning behavior in isolated giant plasma membrane vesicles (GPMVs) with coexisting liquid-ordered (Lo) and liquid-disordered (Ld) phases (Figure 3). To quantify this effect, GPMVs were prepared from cells expressing anchors under conditions shown previously to preserve protein palmitoylation (Levental et al., 2010). GPMVs were imaged using epi-fluorescence microscopy under conditions where vesicles robustly separate into coexisting Lo and Ld phases, visualized by a fluorescent lipid analog with strong

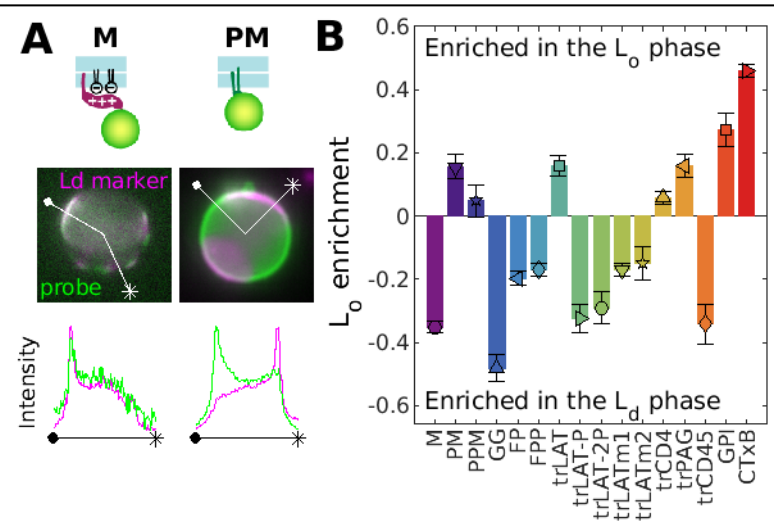


**Figure 3: Anchored probes differentially partition with respect to Lo and Ld phases in isolated GPMVs.** (A) Schematic representation of anchors from Fig 1 with fluorescence images of phase separated GPMVs showing anchor fluorescence (green) alongside a fluorescent marker for the Ld phase (DiO or DiI, magenta). Line scans show the fluorescence intensity in both channels along the trajectory shown. Similar images for all anchored probes are shown in Supplementary Figure S7. (B) Quantification of the Lo phase enrichment of anchors. Error bars show SEM over multiple vesicles and experiments.

preference for the Ld phase (DiO or DiI). Representative images of isolated GPMVs with M and PM anchors are shown in Fig 3A, and representative images for all anchors are included in Supplementary Figure S7. Phase partitioning is quantified by measuring the background-corrected fluorescence intensity of anchors in the two phases, which is proportional to their concentration. Anchor enrichment in the Lo phase is calculated from line-scans through intensity images of the vesicle mid-plane (as in Fig 3A) according to: ([Lo]-[Ld])/([Lo]+[Ld]). This quantity is bounded by -1 for an anchor that is exclusively present in the Ld phase and 1 for probes exclusively present in the Lo phase. At least 10 vesicles across at least 3 separate experiments are used to produce the Lo enrichment values shown in Fig 3B.

The trends observed across anchors are in good qualitative agreement with expectations from past findings (Diaz-Rohrer et al., 2014; Levental et al., 2010; Lorent et al., 2017). In particular, palmitoylation is required but not sufficient for enrichment in the Lo phase for both transmembrane and inner leaflet peripheral anchors. Src family kinase anchors that are both palmitoylated and myristoylated are more strongly enriched in Lo domains than Ras family anchors that are palmitoylated and prenylated. For transmembrane anchors, both palmitoylation and the sequence of the transmembrane helix impact the magnitude of Lo phase enrichment. GPI and CTxB anchors that localize exclusively to the outer leaflet both enrich strongly in the Lo phase.

**Probe concentration in BCR clusters is quantitatively predicted by GPMV phase partitioning**

Figure 4A directly compares anchor partitioning near BCR clusters in live B cells (Δc(r<50nm)) with anchor enrichment in Lo phase domains of isolated GPMVs (Fig 3B). There is a statistically significant correlation between partitioning to Lo domains in GPMVs and to BCR clusters in cells when all anchors are considered together (p=0.004; Fig 4A). Here, the scatter of the points around the linear trend is larger than expected given the error bounds of individual measurements, indicating that Lo phase enrichment is only one of multiple factors contributing to anchor co-localization with BCR. Similar plots showing probe enrichment in cells with unclustered or clustered BCR (c(r<50nm)) are included in Supplementary Figure S8.

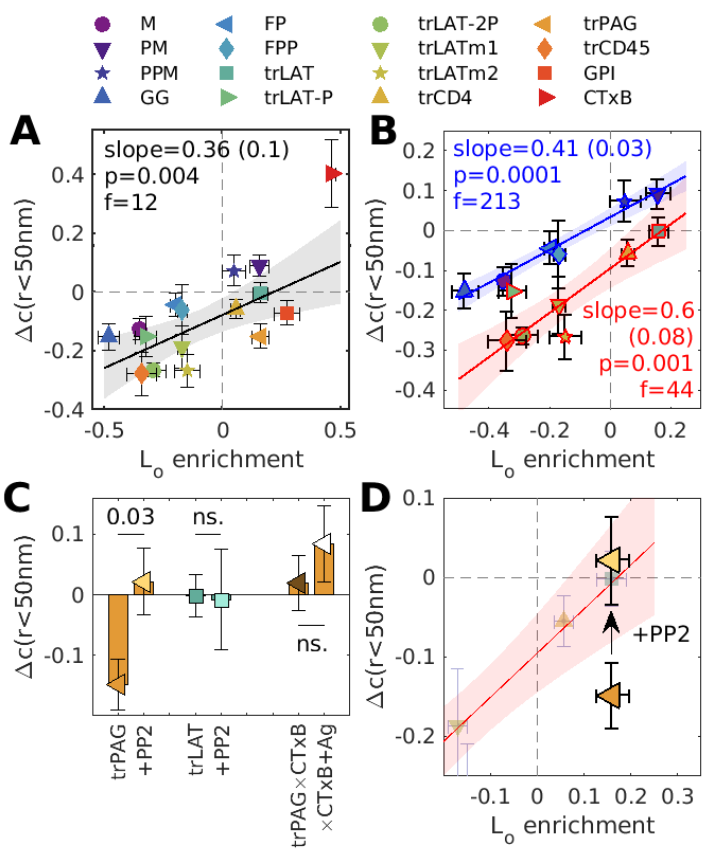


**Figure 4: Anchor concentrations near receptor clusters are quantitatively predicted by GPMV measurements**. (A) Changes in the magnitude of co-clustering between anchors and BCR upon clustering in cells (Δc(r<50nm) from Fig 2B) plotted vs. Lo enrichment in isolated GPMV (Fig 4B). (B) A subset of the data in A, separated by anchor class with peripheral anchors at the inner leaflet outlined in blue and transmembrane peptides outlined in red. Trends in A, B are fit to a linear model and the significance is assessed with a p-value vs. the null hypothesis of no correlation (lower values indicate greater significance), and an f-statistic that describes how well the variance in the data is described by the linear fit (higher values indicate greater significance). Shaded regions in A-B indicate the 95% confidence interval of the linear fit. (C) Changes in cross-correlation amplitudes (Δc(r<50nm)) for the specified probe-pairs both in the presence and absence of pre-treatment with PP2. trPAG was also imaged alongside clustered CTxB (×CTxB) in cells with (+Ag) and without BCR clustering. (D) PP2 treatment brings trPAG partitioning in-line with the correlations for transmembrane anchors redrawn from B.

The significance of the linear model increases substantially when points corresponding to peripheral anchors and transmembrane anchors are considered separately (Fig 4B). Moreover, the scatter of the points away from the linear trend is consistent with experimental error, indicating that Lo phase partitioning in GPMVs is sufficient to explain the observed enrichment in BCR clusters (or vice versa) within these anchor classes. The linear model describing inner leaflet peripheral anchors passes close to the point (0, 0), indicating that peripheral probes that partition equally between phases in GPMVs also show no preference for BCR clusters. The linear model describing transmembrane peptides is systematically shifted to lower values across the whole range of GPMV ordered phase affinities, indicating that transmembrane anchors experience a repulsive force from BCR clusters beyond that experienced by peripheral anchors. We speculate that this additional repulsive interaction arises from steric hindrance of transmembrane domains within the crowded transmembrane environment at the center of these clusters. The slopes of these linear trends are close to 0.5, indicating that the magnitude of probe enrichment or depletion at BCR clusters is half that of Lo domains in GPMVs. When the impact of finite resolution is estimated through deconvolution, these slopes increase (0.55±0.04 for peripheral probes and 0.7±0.2 for transmembrane probes) while retaining high significance (Supplementary Figure S5), indicating that the center of BCR clusters more closely resembles Lo domains in GPMVs than indicated in Fig 4B.

Fig 4B omits the trPAG anchor whose preference for BCR clusters in cells represents a clear outlier from the linear trend. trPAG is markedly excluded from BCR clusters even though it partitions with Lo domains in isolated GPMVs to a similar degree as trLAT. trPAG is derived from the transmembrane domain of PAG/CBP, an adaptor protein that plays important roles in downregulating BCR signaling (Kalland et al., 2012). Based on the functional role of the full length protein, we hypothesized that signaling-dependent effects could account for trPAG exclusion from BCR clusters at the early activation time-points explored. In support of this hypothesis, we found that trPAG is not excluded from BCR clusters formed in the presence of the Src kinase inhibitor PP2, even though this treatment does not impact the distribution of trLAT (Fig 4C), bringing $\Delta c(r<50nm)$ for trPAG into agreement with the trend of Fig 4B (Fig 4D). We also find that trPAG enriches in ordered domains stabilized by clusters of CTxB both before and after BCR clustering (Fig 4C), indicating that the phase preference of trPAG is not directly impacted by BCR activation. Instead, we find that BCR activation leads to the recruitment of trPAG to adhesive structures labeled by Focal Adhesion Kinase (Supplementary Figure S9) through an unknown mechanism.

**Anchors exhibit diverse mobility on the B cell surface**

Fluorescent localizations used to characterize BCR and anchor spatial distributions can also be used to quantify anchor mobility by measuring the temporal evolution of the anchor's auto-correlation function, $g(r, \tau)$. $g(r, \tau)$ reports on the probability of finding pairs of localizations of the *same* molecule type separated by a distance r and a time-interval $\tau$. This approach is similar to quantifying diffusion using single particle tracking (SPT) but has the advantage that segments are not explicitly linked to build trajectories, enabling unambiguous determination of mobility parameters when probes are imaged at high density.

$g(r)$ at each $\tau$ is minimally described as a superposition of two states, one slow and one fast, with distinct mean squared displacements (MSDs) extracted by fitting $g(r)$ at each $\tau$ to a superposition of Gaussian functions. This is shown for a representative trLAT-expressing cell in Figure 5A and fit parameters for the same cell are shown in Fig 5B. The slower state produces a smaller $MSD(\tau)$ that does not vary meaningfully with time-interval, indicating that it is confined. The percentage of molecules in this state ($\alpha$) is a small portion of the total population of molecules ($\alpha<5\%$) and this MSD can be converted to a confinement radius ($r_c=sqrt(MSD)$). The faster population exhibits a larger MSD that is nearly linear over a broad range of time-intervals ($15 \leq \tau \leq 200ms$). This MSD can be converted to a diffusion coefficient (D) that decreases somewhat as $\tau$ increases, indicating that this population is mobile though slightly sub-diffusive. Although absolute values differ, confined and mobile diffusive states with the qualities described above for trLAT in this single cell are representative of those observed for all cells and anchors. Several other examples are provided in Supplementary Figure S10.

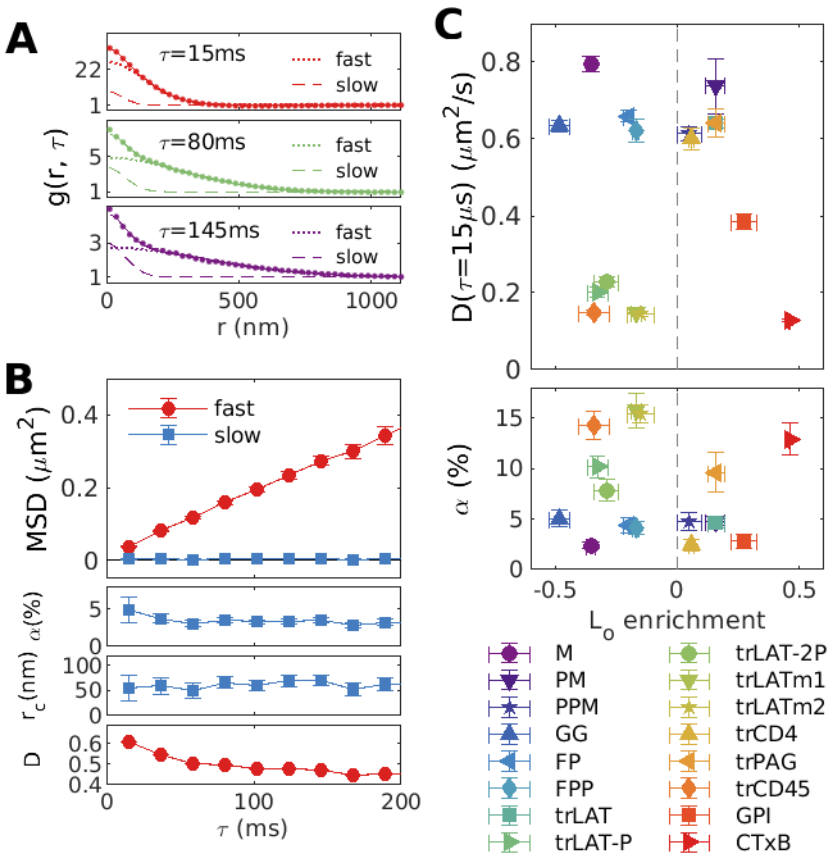


**Figure 5: Absolute anchor mobility is not predicted by Lo enrichment.** (A) Spatial auto-correlation functions (g(r, τ)) for trLAT in a single cell at different time-intervals τ (points). These curves are fit to a super-position of two Gaussian functions (sum as solid lines, individual states with dashes as indicated) to extract mean squared displacements (MSDs) and immobile fractions (α) for each τ. (B) Plots of fit parameters for cell shown in A. MSD of the confined population is converted to a confinement radius ($r_c$=sqrt(MSD)) and the MSD of the mobile component is converted to a Diffusion coefficient (D). (C) D and α evaluated at the first time-interval (τ=15ms) plotted against the Lo enrichment of anchors in GPMVs (values from Fig 3B).

Figure 5C shows a summary of the diffusion coefficient of the mobile state and the percentage of confined molecules evaluated at the shortest time-interval (τ=15ms), averaged over all cells for each anchor. There is no clear trend between the mobility parameters for each anchor and Lo enrichment in GPMVs. Instead, probe mobility differs according to probe class. Peripheral peptides bound to the inner leaflet exhibit the fastest mobility ($D > 0.6\ \mu m^2/s$) and the lowest fraction of confined molecules ($\alpha \leq 5\%$) while the majority of transmembrane peptides exhibit slower mobility ($D < 0.3\ \mu m^2/s$) and higher fractions of confined molecules ($\alpha > 5\%$). GPI on the outer leaflet exhibits an intermediate mobility and few confined molecules, while CTxB diffuses the slowest of all anchors ($D=0.13\ \mu m^2/s$), with a large fraction of confined molecules (α=13%). Among the transmembrane anchors, trLAT, trCD4, and trPAG exhibit the highest mobility, and also share a common topology where the fluorescent protein is located on the intracellular side of the anchor. For trLAT and trCD4, repositioning the fluorophore to face the extracellular space results in mobility similar to all other transmembrane anchors (Supplementary Figure S11).

Together, the findings of Figure 5C indicate that ordered domain affinity does not determine anchor mobility within error bounds and at the time-scales probed. Rather, the mode of membrane anchoring and the position of the fluorescent protein are the major determinants of anchor diffusivity and confinement. This is in good general agreement with past work showing that membrane protein mobility is dictated by the size and shape of the anchor, the density and type of obstacles, and the viscosity of the embedding membrane (A. Camley and H. Brown, 2013; Fujiwara et al., 2002; Guigas and Weiss, 2016; Kenworthy et al., 2004; Knight et al., 2010; Saffman and Delbrück, 1975). A summary of all fit parameters extracted from probes imaged both before and after BCR cross-linking are supplied in Supplementary Figure S12.

**Lo phase enrichment predicts relative anchor mobility.**

We next asked if BCR clustering and subsequent cellular activation alters anchor mobility, and if this effect correlates with Lo affinity. Figure 6A shows how the average diffusion coefficient varies with τ for GG and PPM, two anchors with similar absolute mobility but disparate partitioning behavior. For GG, BCR activation results in a small but systematic

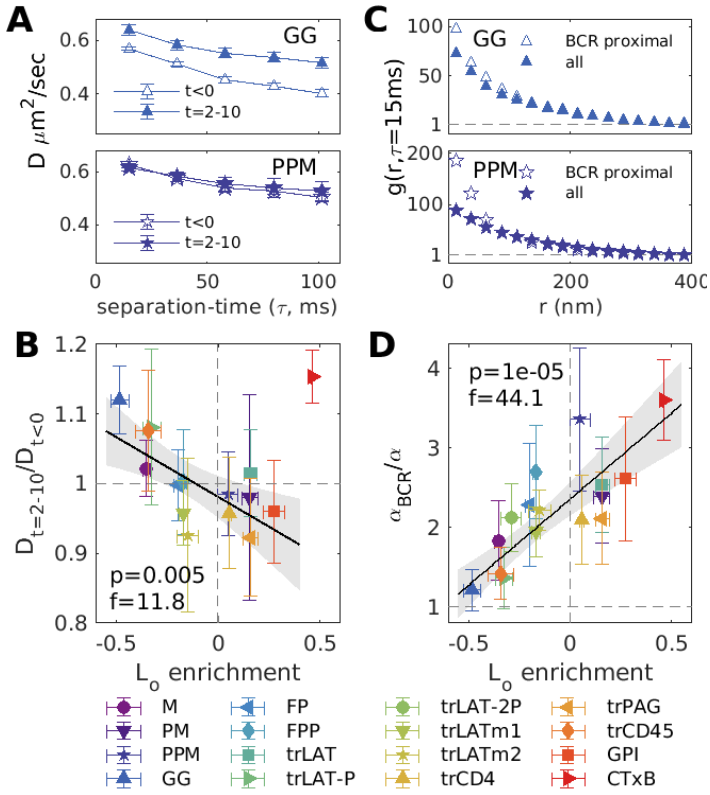


**Figure 6: Relative anchor mobility is predicted by Lo enrichment.** (A) The diffusion coefficient (D) of the mobile fraction as a function of separation time τ from images acquired before (t<0min) and after (t=2-10min) BCR crosslinking. Points are averages over all cells imaged and errors are the SEM between cells. (B) Ratios of diffusion coefficients before and after BCR crosslinking for τ=15ms. The point corresponding to CTxB (red triangle) is excluded from the linear fit. A similar plot comparing α before and after crosslinking is presented in Supplementary Figure S13. (C) g(r, τ) functions showing the mobility of all anchors (all) or the subset of anchors localized within 100nm of a BCR cluster (BCR proximal) at τ=15ms. Curves are averages over all cells expressing the specified probe imaged 2-10min after BCR clustering. (D) Ratios of the confined fractions for all anchors (α) and BCR proximal anchors ($\alpha_{BCR}$) for τ=15ms. All points are included in the linear fit, but trLAT-2P is excluded from this plot due to poor statistics in unstimulated cells. A similar plot comparing D overall to D proximal to BCR is in Supplementary Figure S13. Trends in B, D are fit to a linear model and the significance is assessed with a p-value and an f-statistic as described in Fig 4. Shaded regions in B, D indicate the 95% confidence interval.

shift to larger diffusion coefficients (faster diffusion) across time-intervals, while diffusion coefficients are unchanged by cellular activation for PPM. The ratios of diffusion coefficients before and after BCR clustering for all anchors are summarized in Fig 6B, revealing a statistically significant correlation with Lo enrichment in GPMVs. BCR activation results in faster diffusion for anchors that partition to Ld domains (Lo enrichment<0), while diffusion is slower or remains unchanged for anchors that prefer Lo domains (Lo enrichment>0). This approach interrogates anchors imaged across the cell surface, with the vast majority of anchors localized away from BCR clusters. Thus, the direct physical impact of BCR clusters is likely minimal. Rather, it seems likely that stimulation-induced changes, such as in actin structure and cytoskeleton-membrane coupling, may contribute to the observed trend. Past work indicates that stimulation results in a reduction in ERM protein engagement with the plasma membrane (Pore and Gupta, 2015), suggesting that these actin-membrane contacts present greater barriers to the diffusion of Ld-favoring components (Machta et al., 2011). We also find that anchor confinement is reduced for anchors overall after BCR activation, and that Lo enriched anchors experience the greatest reduction in confinement, again supporting the hypothesis that actin-engaged structures tend to favor Lo domains (Supplemental Figure S13). A clear outlier to the trend of Fig 6B is CTxB, which diffuses faster after B cell activation while strongly partitioning to the Lo phase in GPMVs. Past work suggests that diffusion of this anchor is dependent on membrane curvature (Kabbani et al., 2020), which is not likely to impact the mobility of other anchors due to their small size, and it is possible that stimulation- or time-dependent changes in curvature contribute to the observed behavior.

We next compared the mobility of all anchors in stimulated cells to the subset of anchors that pass within 100 nm of a BCR cluster to isolate effects on diffusion that may arise from the distinct membrane regions around clustered receptors. Fig 6C shows how correlation curves for BCR-proximal probes compare to curves generated from all probe localizations at τ=15ms for GG and PPM. In both cases, the most notable effect is that BCR-proximal anchors have increased auto-correlation amplitudes at short r, indicating that anchors are more likely to travel short distances near BCR clusters. Fitting correlation functions for BCR-proximal anchors indicates that this change can be attributed to a larger population of confined anchor molecules close to BCR clusters ($\alpha_{BCR}$) than are present in the membrane overall (α) without meaningful changes in the diffusion coefficient of the mobile component (Supplementary Figure S13). A similar

effect is observed across all anchors, although the relative magnitude of the confined population ($\alpha_{BCR}/\alpha$) varies. A highly significant trend is observed when this ratio is considered alongside Lo enrichment measured in GPMVs (Fig 6D). Specifically, the most Lo-enriched anchors are 3-4 times more likely to be confined near a BCR cluster than in the membrane overall, while strongly Ld-enriched anchors are minimally impacted by the presence of a BCR cluster. This trend holds despite the lack of a significant correlation between Lo partitioning and either $\alpha$ or $\alpha_{BCR}$ when considered individually (Supplementary Figure S12). This striking relationship suggests that stabilization of an ordered membrane environment around clustered BCR can control not only recruitment but also the retention of relevant membrane components.

## DISCUSSION

Here we present a systematic comparison of anchor organization in parallel but independent experiments in cells and vesicles. Clustering the BCR leads to assembly of a signaling platform with a distinct protein and lipid composition establishing a local membrane environment that could facilitate functional interactions between signaling proteins. We show that membrane-mediated forces are sufficient to alter composition proximal to BCR, with membrane-anchored probes recruited or excluded from these signaling platforms despite the absence of any specific protein interaction domains (Fig 1). A role for phase separation naturally emerges because a diversity of membrane anchoring motifs are examined and because quantitative methods can directly measure protein concentration in both systems, the parameter that is determined by the thermodynamics of this phase transition.

We observe a remarkable convergence between observations of probe enrichment in BCR clusters (Fig 2) and probe enrichment in Lo domains in isolated GPMVs (Fig 3), supporting past implications (Gold and Reth, 2019; Gupta and DeFranco, 2007; Pierce and Liu, 2010; Sohn et al., 2006; Stone et al., 2017) that BCR signaling platforms are extended ordered domains (Fig 4). Even though anchors exhibit diverse mobility in cells (Fig 5), their phase preference predicts changes in mobility upon BCR activation, with enhanced diffusion of Ld components across the membrane and increased dwell times of Lo components near BCR clusters (Fig 6). The partitioning of membrane anchors between Lo and Ld phases in isolated vesicles is predictive of anchor organization and dynamics in intact cells, supporting the conclusion that liquid-liquid phase separation is an organizing principle within cell membranes.

### A new perspective on ordered domains in cell membranes

Our observations, combined with other recent studies (Kinoshita et al., 2017; Koyama-Honda et al., 2020; Li et al., 2020; Stone et al., 2017), put to rest a long history of debate regarding the existence of ordered membrane domains often referred to as 'lipid rafts' in cells. Our findings clearly demonstrate that ordered domains can and do exist in intact cells, that they can emerge in response to stimuli (Fig 1), and that their presence impacts the concentration and dynamics of membrane proteins (Figs 4,6). Although macroscopic separation of Lo and Ld phases does not occur in intact plasma membranes, insights from model membranes explain how phase separation underlies emergent structure in living systems.

Nanoscale heterogeneity has been consistently reported in model membranes that can be driven to macroscopic phase separation through modest changes in temperature or composition (Bloom and Thewalt, 1995; Heberle et al., 2010; Ingólfsson et al., 2014; Oldfield and Chapman, 1972; Pathak and London, 2015). Past studies (Ge et al., 2003; Veatch et al., 2008), including several recent contributions (Heberle et al., 2020; Li et al., 2020; Schneider et al., 2017), demonstrate that nanoscopic structure also exists in isolated plasma membranes, even where no macroscopic phase separation can be observed. Past work also indicates that the length scale of domains can be extended from the nano to the micron scale through external forces acting on membranes. For example, lipid probes that prefer Lo or Ld phases can be sorted by regions of high curvature in single phase membranes close to a miscibility phase transition even in the absence of proteins, and this effect is amplified when proteins are included that couple to both curvature and

membrane phases (Heinrich et al., 2010; Sorre et al., 2009). Extended phase-selective domains also form when proteins or lipids are clustered through adhesion (Zhao et al., 2013) or when membranes are coupled to protein complexes (Liu and Fletcher, 2006; Manley et al., 2008), cytoskeletal scaffolds (Arumugam et al., 2015; Honigmann et al., 2014; Vogel et al., 2017), or phase separated protein droplets (Chung et al., 2021; Lee et al., 2019). While the detailed physical mechanisms underlying these phenomena remain an area of active debate (Schmid, 2017), it is clear that single phase model membranes near macroscopic Lo-Ld phase transitions are highly susceptible to perturbations that organize components with specific phase preferences. Our results demonstrate that the same principle extends to living cell membranes.

While membrane phase separation contributes to the composition of BCR clusters, these domains are not held together solely by phase-mediated interactions (Gauld et al., 2002; Mattila et al., 2016; Packard and Cambier, 2013; Tolar et al., 2009). As such, they exhibit properties that differ from coexisting phases in isolated vesicles. In our results, this difference manifests in reduced magnitude of enrichment/depletion of anchors in BCR clusters compared to phase separated domains within vesicles (Fig 4). Similar effects are evident in model membranes with extended stabilized domains, where the contrast of phase-marking probes is reduced when the membrane is further from its macroscopic miscibility phase transition (Sorre et al., 2009; Zhao et al., 2013). The reduced contrast between enrichment in Lo phases of isolated plasma membrane vesicles and BCR clusters is 2-fold (slopes are 0.4 and 0.6 in Fig 4B). Part of this reduced contrast comes from the small size of BCR clusters (r ~35nm, Supplementary Figure S4) being close to the resolution limit of these measurements. When the effect of finite resolution is estimated using a conservative approach, the contrast more closely resembles that of phase separated domains (slopes are 0.5 and 0.7 Sup. Fig S5).

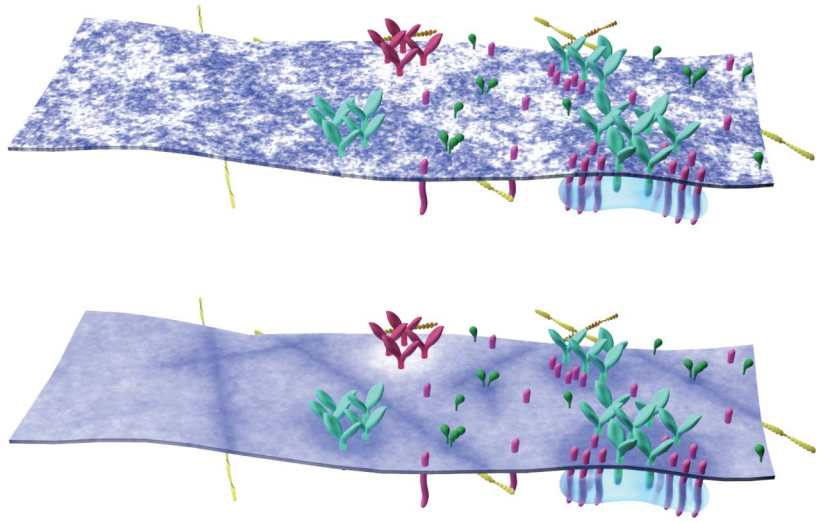

**Figure 7: A model for adaptive membrane organization.** Nanoscale membrane domains preferentially assemble at protein scaffolds to establish functional compartments in the plasma membrane. (top) Instantaneous snapshot of a heterogeneous membrane containing protein structures of increasing complexity, including cortical actin, clustered receptors, adaptor proteins, and membrane proximal signaling assemblies. This membrane contains numerous domains of different sizes and shapes, some of which surround protein rich structures. (bottom) Same membrane drawn above but now membrane composition is averaged over time to show continuous areas of altered local concentration, demonstrating how nano-scale structure can give rise to distinct local membrane environments and define membrane compartments. This is a representation of one specific physical model of membrane heterogeneity (Supplementary Fig S14) but we expect this effect to be general across models.

More generally, we speculate that the marginal loss of contrast inherent to tuning away from macroscopic phase separation is functionally outweighed by the adaptability the membrane acquires in this unique physical state. Near, but not at, phase separation, extended domains similar to phases can assemble or disassemble in response to external stimuli rather than thermodynamic parameters of the membrane itself (Figure 7). Protein assemblies coupled to membranes localize and extend existing nanoscale structure, establishing functional compartments that are stable in both space and time. Thermodynamic parameters of the membrane still play an important role by tuning the magnitude of membrane phase-mediated interactions, changing the composition of domains and modulating interactions between membrane components (Machta et al., 2012). In isolated vesicles, numerous factors impact the location of the macroscopic phase boundary, including cell type, perturbations to lipid homeostasis, incorporation of drugs, and the presence or loss of leaflet asymmetry (Cammarota et al., 2020; Levental et al., 2017, 2020b; Machta et

al., 2016; St. Clair et al., 2020). In principle, these factors may all be used by cells to tune the magnitude of phase-mediated enrichment during cellular processes.

**Stabilized domains in signaling function**

BCR clustering acts to stabilize a membrane domain that influences the local concentrations of membrane components based on their phase preferences (Fig 4). These results support our previous proposals that ordered domain stabilization can be a mechanism for BCR activation, by modifying the access of signaling effectors to receptors (Stone et al., 2017). Receptor kinases and their minimal anchors are enriched in BCR domains, whereas phosphatases and their minimal anchors are excluded. This effect could offset the balance of kinase-phosphatase activity to favor receptor tyrosine phosphorylation and propagation of the activation signal. The relatively slow dynamics of the emergent peptide sorting (Fig 1 C-D) and the observation that ordered domains surrounding BCR clusters extend far beyond the BCR cluster itself (Figs 1B and 2A) suggest that domains are also stabilized by factors that assemble downstream of receptor activation.

Changes in mobility imposed by domains may be another factor that influences signaling interactions. In many cases, the kinetics of interactions between signaling partners set the threshold for cellular activation in response to stimuli, where productive events require sustained assembly of a signaling complex that increases interaction dwell times. This concept is invoked by kinetic proofreading and kinetic segregation models of T cell receptor activation (Davis and van der Merwe, 2006; Ganti et al., 2020; McKeithan, 1995; Tischer and Weiner, 2019; Yousefi et al., 2019). Partitioning-dependent confinement of membrane anchors (Fig 6 C-D) increases their dwell time within domains, potentially increasing the probability of serial engagement and biasing signaling pathways towards activation.

As a general factor influencing membrane organization, phase separation likely has a broad role in spatial regulation of membrane signaling pathways beyond those of clustered receptors. Lo partitioning is a direct consequence of anchor protein structure and posttranslational modification (Levental et al., 2010; Lorent et al., 2017), providing a possible explanation for why protein family members with similar catalytic domains but different membrane anchoring motifs accomplish different cellular functions. Through their particular anchors, membrane proteins can gain preferential access to different membrane compartments defined by the local membrane environment. Mutual affinity for membrane compartments effectively increases interactions between individual protein molecules, impacting their biochemistry and ultimately their functions. Because phase separation is equally able to enrich order- and disorder-preferring membrane components, we anticipate that both ordered and disordered compartments can regulate productive signaling.

The ordered domain established by BCR clusters is likely just one example of domains stabilized by signaling complexes in the plasma membrane. Indeed, any structure that contacts the membrane can in principle couple to a specific membrane compartment, presenting intriguing possibilities about how extended structures such as the actin cytoskeleton can broadly regulate membrane signaling pathways via interactions with membrane microstructure. For example, membrane-cytoskeleton contact sites that preferentially associate with a particular membrane compartment would influence the organization and dynamics of essentially all proteins throughout the membrane plane, based on their phase preferences (as sketched in Fig 7) (Machta et al., 2011). Changes in network structure, i.e. actin dynamics or ERM protein engagement, would produce global changes in membrane organization, impacting interactions across the cell surface (Shelby et al., 2016). Such changes to actin networks occur during signaling through the BCR (Pore and Gupta, 2015), and it seems likely that the changes observed in overall anchor mobility after BCR crosslinking (Fig 6B and Supplementary Figure S13) are a result of changes in actin coupling. While past work focuses primarily on the role of actin in restricting the mobility of specific proteins (Gasparrini et al., 2016), it seems possible that global changes in membrane domains could also play functional roles. Global changes in membrane domains are also expected when thermodynamic parameters within the membrane are altered, as could happen in response to slow changes in lipid metabolism or abrupt changes that occur during the cellular signaling response such as the loss of lipid asymmetry (Elliott et al., 2006) or the enzymatic conversion between lipid species (Marshall et al., 2000).

In summary, we propose a new perspective on membrane domains in cellular processes. This view presents a refinement of the traditional picture of rafts as stable, pre-existing domains that can grow or coalesce in response to stimuli. Instead, we envision membrane phases acting as an adaptive solvent that is highly susceptible to forces acting in and on membranes. This solvent impacts the local concentration and dynamics of proteins within domains, shifting the balance of biochemical reactions and therefore membrane-mediated functions. These domains are sufficient to sort membrane components based on their phase preference even when components lack direct interactions with clustered proteins, and this sorting is sensitive both to external cues and to thermodynamic parameters within the membrane. In this way, the plasma membrane phase transition works in concert with other organizing principles to facilitate and modulate cell function.

**ACKNOWLEDGEMENTS**

We thank Ben Machta, Thomas Shaw, Isabella Graf for helpful conversations. Research was supported by grants from the NIH (GM110052 to SLV, GM134949 and GM124072 to IL), the NSF (MCB1552439 to SLV), the American Cancer Society (PF1800401CCE to SAS), the Volkswagen Foundation (grant 93091 to IL), and the Human Frontiers Science Program (RGP0059/2019 to IL).

**AUTHOR CONTRIBUTIONS**

Conceptualization, SAS and SLV; Methodology, SAS,IL, SLV; Investigation, SAS and ICS, Formal Analysis, SAS and SLV, Resources KW and IL, Writing – original draft, SAS and SLV; Writing – review and editing, SAS, IL, SLV; Visualization, SAS and SLV; Supervision, IL and SLV;

**DECLARATION OF INTERESTS**

The authors declare no competing interests.

**FIGURE LEGENDS**

**Figure 1: BCR clustering produces membrane domains that differently sort two fluorescent proteins anchored at the inner leaflet.** **Figure 1: BCR clustering produces membrane domains that differently sort two fluorescent proteins anchored at the inner leaflet.** (A) Reconstructed live-cell super-resolution images of CH27 B cells imaged between 2 and 10 min after BCR clustering. B cells expressing mEos3.2 conjugated to either a palmitoylated and myristoylated anchor (PM) or a myristoylated anchor (M) (green) are labeled with biotinylated and SiR labeled Fab anti-IgMμ (magenta) that is crosslinked with soluble streptavidin. (B) Quantification of BCR-anchor co-distributions both before (<0min) and after (2-10min) streptavidin addition via the spatial-temporal cross-correlation function c(r, τ) extrapolated to τ=0. Values of $c(r,\tau \to 0) = 1$ indicate a random co-distribution, $c(r,\tau \to 0) > 1$ indicate co-clustering, and $c(r,\tau \to 0) < 1$ indicate exclusion. (C) Images of the region of interest from A reconstructed from 2min of acquired data centered at the time indicated. Time-lapse movies for these cells showing single molecule motions or reconstructed images are included as Supplementary Movies 1-6. (D) The value of the $c(r,\tau \to 0)$ in the first spatial bin (r<50nm) as a function of stimulation time averaged over 5 cells each expressing either PM or M. Cross-correlation amplitudes are evaluated using 2min of acquired localizations centered at the time indicated, as in C. Lines are drawn to guide the eye and are not a fit to any theory. Scale-bars are 10μm in A and are 1μm in A insets and C.

**Figure 2: Anchored probes differentially partition with respect to clustered B cell receptors in live cells.** (A) Schematic representation of anchors used in this study alongside representative reconstructed images showing anchor

fluorescence (green) and BCR (magenta). The trace shows the change in c(r) between anchors and BCR for times between 2 and 8 min after BCR clustering and the curve obtained for times before BCR clustering, which we call Δc(r). Error bounds indicated by the shaded region represent the SEM over cells. (B) Summary of Δc(r) for separation distances less than 50nm. Δc(r<50nm) =0 indicates the anchor does not change its co-distribution with respect to BCR when BCR is clustered, Δc(r<50nm) >0 indicates anchors become more enriched near BCR after clustering, and Δc(r<50nm) <0 indicates anchors become more depleted near BCR after clustering.

**Figure 3: Anchored probes differentially partition with respect to Lo and Ld phases in isolated GPMVs.** (A) Schematic representation of anchors from Fig 1 with fluorescence images of phase separated GPMVs showing anchor fluorescence (green) alongside a fluorescent marker for the Ld phase (DiO or DiI, magenta). Line scans show the fluorescence intensity in both channels along the trajectory shown. Similar images for all anchored probes are shown in Supplementary Figure S7. (B) Quantification of the Lo phase enrichment of anchors. Error bars show SEM over multiple vesicles and experiments.

**Figure 4: Anchor concentrations near receptor clusters are quantitatively predicted by GPMV measurements**. (A) Changes in the magnitude of co-clustering between anchors and BCR upon clustering in cells (Δc(r<50nm) from Fig 2B) plotted vs. Lo enrichment in isolated GPMV (Fig 4B). (B) A subset of the data in A, separated by anchor class with peripheral anchors at the inner leaflet outlined in blue and transmembrane peptides outlined in red. Trends in A, B are fit to a linear model and the significance is assessed with a p-value vs. the null hypothesis of no correlation (lower values indicate greater significance), and an f-statistic that describes how well the variance in the data is described by the linear fit (higher values indicate greater significance). Shaded regions in A-B indicate the 95% confidence interval of the linear fit. (C) Changes in cross-correlation amplitudes (Δc(r<50nm)) for the specified probe-pairs both in the presence and absence of pre-treatment with PP2. trPAG was also imaged alongside clustered CTxB (×CTxB) in cells with (+Ag) and without BCR clustering. (D) PP2 treatment brings trPAG partitioning in-line with the correlations for transmembrane anchors redrawn from B.

**Figure 5: Absolute anchor mobility is not predicted by Lo enrichment.** (A) Spatial auto-correlation functions (g(r, τ)) for trLAT in a single cell at different time-intervals τ (points). These curves are fit to a super-position of two Gaussian functions (sum as solid lines, individual states with dashes as indicated) to extract mean squared displacements (MSDs) and immobile fractions (α) for each τ. (B) Plots of fit parameters for cell shown in A. MSD of the confined population is converted to a confinement radius ($r_c$=sqrt(MSD)) and the MSD of the mobile component is converted to a Diffusion coefficient (D). (C) D and α evaluated at the first time-interval (τ=15ms) plotted against the Lo enrichment of anchors in GPMVs (values from Fig 3B).

**Figure 6: Relative anchor mobility is predicted by Lo enrichment.** (A) The diffusion coefficient (D) of the mobile fraction as a function of separation time τ from images acquired before (t<0min) and after (t=2-10min) BCR crosslinking. Points are averages over all cells imaged and errors are the SEM between cells. (B) Ratios of diffusion coefficients before and after BCR crosslinking for τ=15ms. The point corresponding to CTxB (red triangle) is excluded from the linear fit. A similar plot comparing α before and after crosslinking is presented in Supplementary Figure S13. (C) g(r, τ) functions showing the mobility of all anchors (all) or the subset of anchors localized within 100nm of a BCR cluster (BCR proximal) at τ=15ms. Curves are averages over all cells expressing the specified probe imaged 2-10min after BCR clustering. (D) Ratios of the confined fractions for all anchors (α) and BCR proximal anchors ($\alpha_{BCR}$) for τ=15ms. All points are included in the linear fit, but trLAT-2P is excluded from this plot due to poor statistics in unstimulated cells. A similar plot comparing D overall to D proximal to BCR is in Supplementary Figure S13. Trends in B, D are fit to a linear model and the significance is assessed with a p-value and an f-statistic as described in Fig 4. Shaded regions in B, D indicate the 95% confidence interval.

**Figure 7: A model for adaptive membrane organization.** Nanoscale membrane domains preferentially assemble at protein scaffolds to establish functional compartments in the plasma membrane. (top) Instantaneous snapshot of a

heterogeneous membrane containing protein structures of increasing complexity, including cortical actin, clustered receptors, adaptor proteins, and membrane proximal signaling assemblies. This membrane contains numerous domains of different sizes and shapes, some of which surround protein rich structures. (bottom) Same membrane drawn above but now membrane composition is averaged over time to show continuous areas of altered local concentration, demonstrating how nano-scale structure can give rise to distinct local membrane environments and define membrane compartments. This is a representation of one specific physical model of membrane heterogeneity (Supplementary Fig S14) but we expect this effect to be general across models.

## METHODS

### Cells

CH27 B-cells (mouse, Millipore Cat# SCC115, RRID:CVCL_7178), a lymphoma-derived cell line (Haughton et al., 1986) were acquired from Neetu Gupta (Cleveland Clinic). CH27 Cells were maintained in culture as previously described (Stone and Veatch, 2015). RBL-2H3 (rat, ATCC CRL-2256; RRID: CVCL_0591) and HEK-293 (HEK) (human, ATCC CRL-1573; RRID: CVCL_0045) cells were purchased from ATCC and cultured in medium containing 89% Eagle's Minimum Essential Medium (EMEM), 10% FCS, and 1% penicillin/streptomycin at 37 °C in humidified 5% CO2.

### Probes and Conjugation

*Constructs:* The majority of anchor constructs used in this study were derived from existing anchor-fluorescent protein fusion constructs, with the fluorescent protein sequence replaced by that of mEos 3.2 via standard molecular cloning. All constructs were expressed through transfection of mammalian expression plasmids. The original plasmids were obtained from a variety of sources, and detailed sequence and source information for all anchor constructs is provided in Supplementary Table 1. FAK-eGFP plasmid DNA was obtained from the Baird-Holowka lab.

*Lipid dyes*: FAST-DiO, FAST-DiI and DiD were purchased from ThermoFisher.

*Antibodies, CTxB, and dyes:* Goat anti-Mouse IgM(μ) Fab fragments were obtained from Jackson Immunoresearch (Jackson ImmunoResearch Labs Cat# 115-007-020, RRID:AB_2338477) and were conjugated with biotin and silicon rhodamine (SiR) NHS esters (Invitrogen: B1582, Spirochrome: SC003) to produce "SiR-biotin-Fab". Non-fluorescent biotin-conjugated Goat anti-Mouse IgM(μ) Fab fragments were also obtained from Jackson Immunoresearch (Jackson ImmunoResearch Labs Cat# 115-067-020, RRID:AB_2338587). Anti-GFP nanobody used to label FAK-eGFP was from Chromotek (Chromotek: gt-250) and was conjugated to JaneliaFluor 646 through incubation with JF646 NHS ester (gift of Luke Lavis, Janelia Farms). Cholera Toxin subunit B (CTxB) was from Sigma (Sigma: C9903) and was conjugated with Cy3B NHS ester (Cytiva: PA63101) or with both SiR and biotin as with SiR-biotin-Fab.

*Dye conjugation of labeling proteins:* Antibodies, Fab fragments, and CTxB were all labeled via NHS ester chemistry using the same basic procedure. Amine-reactive dye succinimidyl esters were added to labeling protein solutions (.5 - 2 mg/ml) in 2 - 8x molar excess from stock solutions in DMSO. Reactions were buffered by 0.01M NaH2PO4 with 0.01M NaH2CO3 at pH 8.5 and proceeded for 1 hr at room temperature with rotation. After incubation, the modified proteins were purified and separated from unbound dye through a gel filtration column (GE Healthcare illustra NAP Columns from Fisher: 45-000-151) in 1X-PBS+1mM-EDTA. The modified proteins were further purified by centrifugation in a Vivaspin-500 Polyethersulfone concentration spin column (Vivaproducts: VS0191, VS0121, VS0131, VS0141) with an appropriate molecular weight cutoff (3k-100k) of approximately half the protein molecular weight or lower. The degree of labeling was estimated using the absorbance spectrum of the conjugated protein.

SiR-biotin-Fab and SiR-biotin-CTxB were conjugated to SiR and biotin using a two-step procedure, where first unlabeled proteins were reacted with a mixture of SiR and biotin NHS esters in 5x and 12x molar excess, respectively, and purified as described above. A second round of labeling with SiR NHS ester alone was then performed, with 10x excess dye for

SiR-biotin-Fab and 4x excess for SiR-biotin-CTxB. The degree of labeling for these conjugates was 2.5 SiR per protein for SiR-biotin-Fab and 2.1 SiR per protein for SiR-biotin-CTxB.

Transient transfection and labeling

CH27 cells were transiently transfected with plasmid DNA encoding membrane anchor constructs by Lonza Nucleofector electroporation (Lonza, Basel, Switzerland) with electroporation program CA-137. Typically, $10^6$ CH27 cells were transfected with 1 µg of plasmid DNA. In most cases, transfected cells were grown on glass-bottom Mattek culture dishes overnight for next-day sample preparation. In some cases, cells were grown overnight in flasks and plated on Mattek dishes on the day of sample preparation. BCR was labeled by incubation with 5 µg/ml SiR-biotin-Fab in culture medium for 10 min at room temperature. For live cell imaging experiments, BCR labeling was performed immediately prior to imaging.

When Cy3B-CTxB was imaged alongside SiR-biotin-Fab-labeled BCR instead of a transiently-expressed anchor construct, Cy3b-CTxB was added to the SiR-biotin-Fab labeling solution at a concentration of 5 µg/ml. When SiR-biotin-CTxB was imaged in conjunction with trPAG, SiR-biotin-CTxB was added at 5µg/ml instead of SiR-biotin-Fab in culture medium for 10 min prior to imaging.

For fixed cell imaging experiments, BCR was labeled with biotin-Fab using the same procedure as live cell imaging experiments. Cells were then rinsed with HEPES-buffered salt solution with BSA (HBSS-BSA: 30mM HEPES, 5.6 mM glucose, 100 mM NaCl, 5 mM KCl, 1 mM KCl, 1 mM MgCl2, 1.8 mM CaCl2, .1% w/v BSA, pH 7.4) and were either chemically fixed or BCR was clustered through addition of 1 µg/ml streptavidin for 6 min. Stimulated and unstimulated samples were rinsed with PBS, then fixed (2% PFA .15% glutaraldehyde in PBS) for 10 min at room temperature. Samples were blocked and permeabilized using block solution (PBS with .5% w/v BSA, .05% v/v fish gelatin, .01% Triton-X 100) for 1 hour. For FAK labeling, cells were transiently transfected with FAK-eGFP plasmid DNA and were labeled with JF646 anti-GFP nanobody (1 µg/ml) for 30 min at room temperature after fixation, permeabilization, and blocking. Samples were then thoroughly rinsed with block solution and imaged.

RBL-2H3 or HEK cells were transiently transfected using nucleofection (Amaxa) according to protocols provided with the reagents. 4–6 h after transfection, cells were washed with PBS and then incubated with serum-free medium overnight. To synchronize the cells, 1 h before preparation of GPMV, the cells were given full-serum medium.

Single molecule imaging of B cells

Imaging was performed using an Olympus IX81-XDC inverted microscope. TIRF laser angles where achieved using a cellTIRF module, a 100X UAPO TIRF objective (NA = 1.49), and active Z-drift correction (ZDC) (Olympus America) as described previously (Stone and Veatch, 2015; Stone et al., 2017). SiR and JF646 were excited using a 647 nm solid state laser (OBIS, 100 mW, Coherent) and Cy3B was excited using a with a 561 nm solid state laser (Sapphire 561 LP or OBIS 561-120FP, Coherent). Photoactivation of mEos3.2 was accomplished with a 405 nm diode laser (CUBE 405-50FP, Coherent) and simultaneously excited with the 561 nm solid state laser. Simultaneous imaging of SiR or JF646 and mEos3.2 or Cy3B was accomplished using a LF405/488/561/647 quadband filter cube (TRF89902, Chroma, Bellows Falls, VT). Emission was split into two channels using a DV2 emission splitting system (Photometrics) with a T640lpxr dichroic mirror to separate emission: ET605/52m to filter near-red emission, and ET700/75m to filter far-red emission (Chroma).

Live cell imaging was accomplished at room temperature in a buffer shown previously to be compatible with BCR mediated signaling responses (30 mM Tris, 9 mg/ml glucose, 100 mM NaCl, 5 mM KCl, 1 mM KCl, 1 mM MgCl2, 1.8 mM CaCl2, 10 mM glutathione, 8 µg/ml catalase, 100 µg/ml glucose oxidase, pH 8.5 (Stone et al., 2017). Laser intensities were adjusted such that single fluorophores could be distinguished in individual frames, and were generally between 5-20 kW/cm2 for 561 nm and 647 nm lasers, and 100-200 W/cm2 for the 405 nm laser. Integration times were maintained at 20ms. Generally, 5000 frames (~2min) were acquired in unstimulated cells, then an additional 20,000 frames (8-10min) were acquired after the addition of 1 µg/ml streptavidin, which crosslinks the SiR-biotin-Fab bound to BCR and initiates a signaling response. Throughout imaging, the laser intensity is modulated to maintain a suitable

density of single molecules. For measurements involving treatment with PP2, 5 µM PP2 (Sigma: 529573) from a 10mM stock solution in DMSO was added to culture medium during the SiR-biotin-Fab labeling step prior to imaging. 5 µM PP2 was also added to all imaging buffers so that subsequent imaging and stimulation steps took place in the presence of PP2

Imaging of chemically fixed cells was accomplished with the same illumination and data acquisition settings in a slightly modified buffer (100 mM Tris, 9 mg/ml glucose, 25mM NaCl, 10 mM glutathione, 8 µg/ml catalase, 100 µg/ml glucose oxidase, pH 8.5. Individual fields of view were typically imaged over 20,000 frames, and multiple fields of view were imaged in each prepared dish of cells.

Image Processing and probe Localization

Single molecules were localized in raw live cell movies with the ImageJ plugin ThunderSTORM (Ovesný et al., 2014), using weighted least-squares fitting of an integrated Gaussian PSF with multi-emitter fitting analysis enabled to detect up to 2 single molecules within a diffraction-limited area. Localization data were then exported to our in-house MATLAB software for culling and successive post-processing steps (Veatch et al., 2012). Localizations in the near-red emission channel were registered with the far-red emission channel using a registration technique published previously (Churchman et al., 2005) and previously used by our group (Stone and Veatch, 2014, 2015). Cell regions were masked by hand for further analysis to exclude regions away from the cell as well as regions of extensive topography.

Cross-correlation analysis

Steady-state cross-correlations from live cells were calculated as described previously (Stone and Veatch, 2015), with minor modifications. In brief, cross-correlation functions, c(r ,τ), were computed from localizations in each channel that occurred in the same frame or in frames separated by a time interval τ. Long-range gradients in labeling density arising from diffusing molecules entering the TIR field along with the complicated boundary condition generated by the mask is are accounted for through normalization as follows. For each channel, images reconstructed from data acquired over the entire steady-state time window are convoluted with a Gaussian kernel with σ = 1 µm and masked using the same binary mask applied to localization data. The cross-correlation of the blurred, masked images from each channel is calculated using FFTs and radially averaged as described in (Stone and Veatch, 2015; Veatch et al., 2012) and is used as a normalization factor for c(r ,τ). This treatment filters structure larger than 1 µm in size from the steady-state cross-correlation function.

Bleed-through effects are evident at short τ, and this contribution is removed by fitting c(r ,τ) to a sum of two Gaussian functions for each value of r:

$$\mathrm{c_{observed}}(\mathrm{r}\,,\tau) = 1 + \mathrm{A_{narrow}}\exp\left(-\frac{\tau^2}{4\sigma_{narrow}^2}\right) + \mathrm{A_{broad}}\exp\left(-\frac{\tau^2}{4\sigma_{broad}^2}\right)$$

The standard deviation of the narrow Gaussian function, $\sigma_{narrow}^2$, is constrained by how long it takes an anchor to diffuse through the diffraction limit (taken to be 250nm). This assumes that BCR is less mobile than anchors, which is consistent with experimental observations especially after BCR clustering. The broader Gaussian is interpreted to capture the more slowly varying envelope of the actual c(r, τ), most likely due to slow motions of BCR clusters. Bleed-through is accounted for by excluding the amplitude of the narrow Gaussian function to yield the values reported in the main text:

$$\mathrm{c(r)} = \mathrm{c(r}, \tau \to 0) = 1 + \mathrm{A_{broad}}(r)$$

Several examples of this fitting procedure are shown in Supplementary Figure S1A. This bleed-through correction is not applied for the stimulation-time dependent curves of Fig 1D. For these measurements, the reported values are simply an average over 2s in τ:

$$\mathrm{c(r)} = \langle \mathrm{c(r}, \tau)\rangle_{\tau<2s}$$

This improves statistics while reducing the impact of bleed-through in data with reduced signal to noise and produces results that are very similar to the bleed-through calculation described above, as shown in Supplementary Figure S1B.

Since we consistently observe subtle enrichment of anchors with respect to BCR in cells prior to BCR crosslinking (Supplementary Figure S2), which we attribute to long-lived membrane topography, we report on the enhanced enrichment of probes upon BCR crosslinking in order to isolate the impact of BCR clustering. This is done by subtracting $c(r, \tau \to 0)$ obtained from images acquired prior to BCR crosslinking (t<0) from those acquired between 2-10 min after BCR crosslinking (t=2-10).

$$\Delta c(r) = c_{t=2-10}(r, \tau \to 0) - c_{t<0}(r, \tau \to 0)$$

Δc is tabulated for each cell, and the variance reported in Δc represents the standard error of the mean averaged over cells. For one anchor, trLAT-2P, images were not acquired prior to BCR cross-linking for some cells included in the analysis. In this case, we subtracted the average $c_{t<0}(r, \tau \to 0)$ obtained from cells where this data was present from $c_{t=2-10}(r, \tau \to 0)$ for individual cells.

In Supplementary Figure S5, we estimate the impact of finite resolution and finite BCR cluster size on the amplitude of correlations using deconvolution, to better estimate the enrichment and depletion of anchors with respect to the centers of BCR clusters. Both resolution and the finite size of BCR clusters blur the measured Δc(r), reducing the dynamic range. Deconvolution was accomplished by first spreading Δc(r) over angles to get $\Delta c(\vec{r})$ and a blurring function was estimated as a 2D Gaussian function with standard deviation of 50nm, representing the size of BCR clusters (35nm) and the approximate localization precision of mEos3.2 (35nm) added in quadrature. The 2D deconvolution was accomplished using the deconvlucy function in Matlab, using the blurring function as the point spread function, then $\Delta c_D(\vec{r})$ was averaged over angles to produce $\Delta c_D(r)$. This algorithm assumes and estimates Poisson noise in the measured $\Delta c(\vec{r})$. The same blurring function was used for all cells even though there is some cell to cell variation in localization precision and average BCR cluster size (Supplementary Figure S4) to simplify the analysis. A more careful correction would involve a rigorous estimate of the type and magnitude of noise from each cell and a blurring function specific to each measurement, which was not done here. The average $\Delta c_D(r)$ curves of Figure S5 were tabulated by averaging over $\Delta c_D(r)$ obtained from individual cells. We note that while the dynamic range of these curves increases in magnitude, so does the standard error of the mean between cells at short separation distances.

Determination of Lo enrichment in GPMVs

Cell membranes were stained with 5 µg/ml of FAST-DiO, FAST-DiI or DiD, respectively, green, red or far-red fluorescent lipid dyes that strongly partition to disordered phases (Levental and Levental, 2015). Following staining, GPMVs were isolated from transfected cells as described previously (Sezgin et al., 2012). GPMV formation was induced by 2 mM N-ethylmaleimide (NEM) in hypotonic buffer containing 100 mM NaCl, 10 mM HEPES, and 2 mM $CaCl_2$, pH 7.4. To quantify protein partitioning, GPMVs were observed on an inverted epifluorescence microscope (Nikon) at 4°C after treatment with 200 µM DCA to stabilize phase separation; this treatment has been previously demonstrated not to affect raft affinity of various proteins (Zhou et al., 2013). The relative enrichment of probes in the Lo phase is defined as $(I_o-I_d)/(I_o+I_d)$, where $I_o$ and $I_d$ are baseline corrected fluorescent intensity of the construct in the liquid-ordered and liquid-disordered phases respectively for >10 vesicles/trial, with at least 3 independent experiments for each anchor. This quantity is simply related to the partition coefficient $K_p = I_o/I_d$ as Lo enrichment = $(K_p-1)/(K_p+1)$, but is more appropriate for comparison with cell results because it is normalized to the total concentration rather than the concentration in the Lo phase, as is the case with cross-correlation functions. The majority of measurements were carried out in RBL-2H3 cells, but in some cases HeLa cells were also used due to the enhanced surface expression of some probes in this cell type. When used, partitioning measurements in HeLa cells produced partitioning results that were consistent with those obtained in RBL-2H3 cells but with improved signal to noise.

Fitting to linear models and associated statistics

Cellular results were plotted vs. GPMV probe partitioning data and fit to a linear model to assess the magnitude and significance of correlations. This was done using the function lmfit() in Matlab, and in all cases values were weighted by the inverse variance of the cellular measurement. When ratios were considered, values the stated quantity was tabulated on a cell-by-cell basis and the variance was calculated from the standard error of the mean of the ratio across cells.

The function lmfit() returns a p value against the null hypothesis that the data is described by a constant model (with no linear slope). An ANOVA analysis is then conducted using the anova() function in Matlab. The f-statistic reported is the 'F-statistic vs. constant model' output of this function.

In several instances, significance is reported when comparing two empirical observations. These are conducted using the ttest2 function in Matlab.

Quantification of anchor mobility in cells:

The motion of membrane anchors was quantified from localized single molecule positions using correlation methods as described previously (Stone and Veatch, 2015). Briefly, autocorrelation functions g(r, τ) were tabulated from localized positions as a function of radius r and time interval τ for each cell imaged and normalized following the same protocol as for cross-correlations described above. Correlation functions were tabulated for the same time-windows as for cross-correlation functions, either prior to BCR crosslinking (t<0) or between 2 and 10 min after activation (t=2-10). At each τ, the normalized g(r, τ) was fit to a superposition of two Gaussian functions to extract two distinct mean squared displacements according to the relation:

$$g(r) - 1 = \frac{A_1}{\pi R_1^2} exp\{-r^2/R_1^2\} + \frac{A_2}{\pi R_2^2} exp\{-r^2/R_2^2\}$$

The mean squared displacement (MSD) for each component is related to the fit parameters $R_1$ and $R_2$ which are determined at each τ:

$$MSD_1(\tau) = R_1^2 - 2\langle\sigma_{LP}^2\rangle$$

$$MSD_2(\tau) = R_2^2 - 2\langle\sigma_{LP}^2\rangle$$

Where $\langle\sigma_{LP}^2\rangle$ is the squared localization precision extracted from the single molecule fits and averaged over the complete dataset. The fraction of the population within the first component is $\alpha = A_1/(A_1 + A_2)$.

Several examples of g(r, τ) and fits are shown in Figure 5 and Sup Fig S10 and the average values of fit parameters for all probes are displayed in Sup Fig S12. We refer to the shorter MSD as the immobile component since it does not increase rapidly with τ. The longer MSD increases roughly linearly with τ, consistent with diffusive motion. We have chosen to fit to only two states for simplicity and it is likely that more mobile states are present (Karslake et al., 2020), in which case our single mobile MSD can be interpreted as a weighted average of these states. The fraction of the population within the slow component is determined at each τ and is largely independent of τ, with some exceptions (Sup Fig S10).

The MSD is related to the diffusion coefficient through the relation $MSD(\tau) = 4D(\tau)\tau$. Since fluorophores are illuminated continuously through a finite integration time, images contain information regarding probe locations at different times throughout the integration window. As a result, the effective τ differs from the frame times of the measurement ($\tau_o$) (Berglund, 2010). This is accounted for as follows:

$$\tau = \tau_o\left(1 - \frac{1}{3}\frac{integration\ time}{\tau_o}\right)$$

The integration time was held constant at 20ms for measurements. The frame rate (the smallest value of $\tau_o$) is slightly larger than the integration time and varies across measurements. This correction is largest for short $\tau_o$ when the integration time is almost equivalent to $\tau_o$.

Motions of BCR proximal anchors were isolated from the entire population of anchors by cross-correlating anchor localizations within 100nm of a localized BCR with all anchor localizations. Since BCR clusters are largely immobile after BCR clustering, anchor localizations were included if they passed within 100nm of a BCR localization localized up to 2s previously, which implements the assumption that the BCR cluster remains fixed in space even if a fluorophore labeling BCR is not observed. Cross-correlations of BCR proximal anchors and total anchors were normalized using the same geometrical correction factor used for the cross-correlation of BCR and anchors, since the BCR proximal anchor distribution closely follows that of BCR alone. Spatio-temporal cross-correlation functions were fit to extract mobility parameters following the procedures described above for auto-correlations

Generation of the membrane for Figure 7:

The membrane shown in Fig 7 was generated from a 2D matrix of pixel values (p), half normally distributed around the value -1 and half normally distributed around the value +1. Pixels were allowed to redistribute across the matrix through non-local exchanges and with periodic boundary conditions using a Monte Carlo algorithm that satisfied detailed balance, which tabulates the energy at each position i as $E_i = -\sum_{j=1}^{4} p_i p_j$ where $p_j$ represents the pixel value of the 4 nearest neighbors. Temperature was chosen such that the size of structure in the simulation was small compared to the size of the matrix.

After equilibration, a weak field was introduced to bias the location of pixels within certain regions of the matrix. This field provided the additional energy $Ef_i = -p_i F_i$. Plots showing the distribution of pixel values and the applied field matrix are found in Supplementary Figure S14. The matrix was square (400 by 400 pixels) and the field was applied in a region of the simulation. The remaining values of the field were set to zero. The average image was generated by averaging 50 different simulation snapshots with the same applied field.

**MULTIMEDIA FILES**

**Supplementary Movie 1: Single molecule motions of BCR and PM before BCR crosslinking.** Time-lapse video showing reconstructed single molecule positions evolving in time for BCR (magenta) and PM (green) for the same PM expressing cell shown in Fig 1. A-C. These localizations were acquired <1min prior to the addition of streptavidin. Localizations are drawn on a reconstructed image of all PM localizations for this cell. The movie is displayed with a frame rate that is 5x slower than real time. Scale bar is 5 µm.

**Supplementary Movie 2: Single molecule motions of BCR and PM after BCR crosslinking.** Time-lapse video showing reconstructed single molecule positions evolving in time for BCR (magenta) and PM (green) for the same PM expressing cell shown in Fig 1. A-C. These localizations were acquired ~2min after addition of streptavidin. Localizations are drawn on a reconstructed image of all PM localizations for this cell. The movie is displayed with a frame rate that is 5x slower than real time. Scale bar is 5 µm.

**Supplementary Movie 3: Single molecule motions of BCR and M before BCR crosslinking.** Time-lapse video showing reconstructed single molecule positions evolving in time for BCR (magenta) and M (green) for the same M expressing cell shown in Fig 1. A-C. These localizations were acquired <1min prior to the addition of streptavidin. Localizations are drawn on a reconstructed image of all PM localizations for this cell. The movie is displayed with a frame rate that is 5x slower than real time. Scale bar is 5 µm.

**Supplementary Movie 4: Single molecule motions of BCR and M after BCR crosslinking.** Time-lapse video showing reconstructed single molecule positions evolving in time for BCR (magenta) and M (green) for the same M expressing

cell shown in Fig 1. A-C. These localizations were acquired ~2min after addition of streptavidin. Localizations are drawn on a reconstructed image of all PM localizations for this cell. The movie is displayed with a frame rate that is 5x slower than real time. Scale bar is 5 µm.

**Supplementary Movie 5: Time lapse of BCR and PM organization before and after BCR cross-linking.** Time lapse movie composed of reconstructed images of BCR (magenta) and PM (green) from the same representative cell shown in Fig 1. A-C, shown here at higher time resolution to demonstrate how BCR and PM organization evolve over time. Each sequential image is reconstructed from a window of 750 frames (~20sec) incremented by 250 frames for each image. The entire time lapse spans the length of the live cell experiment and the real time of data acquisition is shown in the bottom-left, where 0 min corresponds to streptavidin addition. Before streptavidin addition, both BCR and PM are relatively uniformly distributed across the plasma membrane. After streptavidin addition, BCR rapidly forms tight clusters. BCR clusters are relatively immobile compared to PM, but do exhibit dynamics that are clearly evident in the time lapse. Scale bar is 5 µm.

**Supplementary Movie 6: Time lapse of BCR and M organization before and after BCR cross-linking.** Time lapse movie composed of reconstructed images of BCR (magenta) and M (green)from the same representative cell shown in Fig 1. A-C. Parameters for reconstruction of individual frames of the time lapse are the same as in Supplementary Movie 3, and the time lapse shows similar organization of BCR and M before and after streptavidin addition. Time before and after streptavidin addition in shown in the bottom left and the scale bar is 5 µm.

**REFERENCES**

A. Camley, B., and H. Brown, F.L. (2013). Diffusion of complex objects embedded in free and supported lipid bilayer membranes: role of shape anisotropy and leaflet structure. Soft Matter *9*, 4767–4779.

Arumugam, S., Petrov, E.P., and Schwille, P. (2015). Cytoskeletal Pinning Controls Phase Separation in Multicomponent Lipid Membranes. Biophys. J. *108*, 1104–1113.

Baumgart, T., Hammond, A.T., Sengupta, P., Hess, S.T., Holowka, D.A., Baird, B.A., and Webb, W.W. (2007). Large-scale fluid/fluid phase separation of proteins and lipids in giant plasma membrane vesicles. Proc. Natl. Acad. Sci. U. S. A. *104*, 3165–3170.

Berglund, A.J. (2010). Statistics of camera-based single-particle tracking. Phys. Rev. E *82*, 011917.

Bloom, M., and Thewalt, J.L. (1995). Time and distance scales of membrane domain organization. Mol. Membr. Biol. *12*, 9–13.

Cammarota, E., Soriani, C., Taub, R., Morgan, F., Sakai, J., Veatch, S.L., Bryant, C.E., and Cicuta, P. (2020). Criticality of plasma membrane lipids reflects activation state of macrophage cells. J. R. Soc. Interface *17*, 20190803.

Chung, J.K., Huang, W.Y.C., Carbone, C.B., Nocka, L.M., Parikh, A.N., Vale, R.D., and Groves, J.T. (2021). Coupled membrane lipid miscibility and phosphotyrosine-driven protein condensation phase transitions. Biophys. J. *120*, 1257–1265.

Churchman, L.S., Ökten, Z., Rock, R.S., Dawson, J.F., and Spudich, J.A. (2005). Single molecule high-resolution colocalization of Cy3 and Cy5 attached to macromolecules measures intramolecular distances through time. Proc. Natl. Acad. Sci. U. S. A. *102*, 1419–1423.

Davis, S.J., and van der Merwe, P.A. (2006). The kinetic-segregation model: TCR triggering and beyond. Nat. Immunol. *7*, 803–809.

Diaz-Rohrer, B.B., Levental, K.R., Simons, K., and Levental, I. (2014). Membrane raft association is a determinant of plasma membrane localization. Proc. Natl. Acad. Sci. U. S. A. *111*, 8500–8505.

Eggeling, C., Ringemann, C., Medda, R., Schwarzmann, G., Sandhoff, K., Polyakova, S., Belov, V.N., Hein, B., von Middendorff, C., Schönle, A., et al. (2009). Direct observation of the nanoscale dynamics of membrane lipids in a living cell. Nature *457*, 1159–1162.

Elliott, J.I., Sardini, A., Cooper, J.C., Alexander, D.R., Davanture, S., Chimini, G., and Higgins, C.F. (2006). Phosphatidylserine exposure in B lymphocytes: a role for lipid packing. Blood *108*, 1611–1617.

Ernst, R., Ejsing, C.S., and Antonny, B. (2016). Homeoviscous Adaptation and the Regulation of Membrane Lipids. J. Mol. Biol. *428*, 4776–4791.

Fujiwara, T., Ritchie, K., Murakoshi, H., Jacobson, K., and Kusumi, A. (2002). Phospholipids undergo hop diffusion in compartmentalized cell membrane. J. Cell Biol. *157*, 1071–1082.

Ganti, R.S., Lo, W.-L., McAffee, D.B., Groves, J.T., Weiss, A., and Chakraborty, A.K. (2020). How the T cell signaling network processes information to discriminate between self and agonist ligands. Proc. Natl. Acad. Sci. *117*, 26020–26030.

Gasparrini, F., Feest, C., Bruckbauer, A., Mattila, P.K., Müller, J., Nitschke, L., Bray, D., and Batista, F.D. (2016). Nanoscale organization and dynamics of the siglec CD22 cooperate with the cytoskeleton in restraining BCR signalling. EMBO J. *35*, 258–280.

Gauld, S.B., Porto, J.M.D., and Cambier, J.C. (2002). B Cell Antigen Receptor Signaling: Roles in Cell Development and Disease. Science *296*, 1641–1642.

Ge, M., Gidwani, A., Brown, H.A., Holowka, D., Baird, B., and Freed, J.H. (2003). Ordered and Disordered Phases Coexist in Plasma Membrane Vesicles of RBL-2H3 Mast Cells. An ESR Study. Biophys. J. *85*, 1278–1288.

Gold, M.R., and Reth, M.G. (2019). Antigen Receptor Function in the Context of the Nanoscale Organization of the B Cell Membrane. Annu. Rev. Immunol. *37*, 97–123.

Guigas, G., and Weiss, M. (2016). Effects of protein crowding on membrane systems. Biochim. Biophys. Acta BBA - Biomembr. *1858*, 2441–2450.

Gupta, N., and DeFranco, A.L. (2007). Lipid rafts and B cell signaling. Semin. Cell Dev. Biol. *18*, 616–626.

Haughton, G., Arnold, L.W., Bishop, G.A., and Mercolino, T.J. (1986). The CH Series of Murine B Cell Lymphomas: Neoplastic Analogues of Ly-1+ Normal B Cells. Immunol. Rev. *93*, 35–52.

Heberle, F.A., Wu, J., Goh, S.L., Petruzielo, R.S., and Feigenson, G.W. (2010). Comparison of Three Ternary Lipid Bilayer Mixtures: FRET and ESR Reveal Nanodomains. Biophys. J. *99*, 3309–3318.

Heberle, F.A., Doktorova, M., Scott, H.L., Skinkle, A.D., Waxham, M.N., and Levental, I. (2020). Direct label-free imaging of nanodomains in biomimetic and biological membranes by cryogenic electron microscopy. Proc. Natl. Acad. Sci. *117*, 19943–19952.

Heinrich, M., Tian, A., Esposito, C., and Baumgart, T. (2010). Dynamic sorting of lipids and proteins in membrane tubes with a moving phase boundary. Proc. Natl. Acad. Sci. *107*, 7208–7213.

Honigmann, A., Sadeghi, S., Keller, J., Hell, S.W., Eggeling, C., and Vink, R. (2014). A lipid bound actin meshwork organizes liquid phase separation in model membranes. ELife *3*.

Ingólfsson, H.I., Melo, M.N., van Eerden, F.J., Arnarez, C., Lopez, C.A., Wassenaar, T.A., Periole, X., de Vries, A.H., Tieleman, D.P., and Marrink, S.J. (2014). Lipid Organization of the Plasma Membrane. J. Am. Chem. Soc. *136*, 14554–14559.

Kabbani, A.M., Raghunathan, K., Lencer, W.I., Kenworthy, A.K., and Kelly, C.V. (2020). Structured clustering of the glycosphingolipid GM1 is required for membrane curvature induced by cholera toxin. Proc. Natl. Acad. Sci. *117*, 14978–14986.

Kalland, M.E., Solheim, S.A., Skånland, S.S., Taskén, K., and Berge, T. (2012). Modulation of proximal signaling in normal and transformed B cells by transmembrane adapter Cbp/PAG. Exp. Cell Res. *318*, 1611–1619.

Karslake, J.D., Donarski, E.D., Shelby, S.A., Demey, L.M., DiRita, V.J., Veatch, S.L., and Biteen, J.S. (2020). SMAUG: Analyzing single-molecule tracks with nonparametric Bayesian statistics. Methods.

Kenworthy, A.K. (2008). Have we become overly reliant on lipid rafts? Talking Point on the involvement of lipid rafts in T-cell activation. EMBO Rep. *9*, 531–535.

Kenworthy, A.K., Nichols, B.J., Remmert, C.L., Hendrix, G.M., Kumar, M., Zimmerberg, J., and Lippincott-Schwartz, J. (2004). Dynamics of putative raft-associated proteins at the cell surface. J. Cell Biol. *165*, 735–746.

Kinoshita, M., Suzuki, K.G.N., Matsumori, N., Takada, M., Ano, H., Morigaki, K., Abe, M., Makino, A., Kobayashi, T., Hirosawa, K.M., et al. (2017). Raft-based sphingomyelin interactions revealed by new fluorescent sphingomyelin analogs. J. Cell Biol. *216*, 1183–1204.

Knight, J.D., Lerner, M.G., Marcano-Velázquez, J.G., Pastor, R.W., and Falke, J.J. (2010). Single Molecule Diffusion of Membrane-Bound Proteins: Window into Lipid Contacts and Bilayer Dynamics. Biophys. J. *99*, 2879–2887.

Koyama-Honda, I., Fujiwara, T.K., Kasai, R.S., Suzuki, K.G.N., Kajikawa, E., Tsuboi, H., Tsunoyama, T.A., and Kusumi, A. (2020). High-speed single-molecule imaging reveals signal transduction by induced transbilayer raft phases. J. Cell Biol. *219*.

Lee, I.-H., Imanaka, M.Y., Modahl, E.H., and Torres-Ocampo, A.P. (2019). Lipid Raft Phase Modulation by Membrane-Anchored Proteins with Inherent Phase Separation Properties. ACS Omega *4*, 6551–6559.

Levental, K.R., and Levental, I. (2015). Isolation of Giant Plasma Membrane Vesicles for Evaluation of Plasma Membrane Structure and Protein Partitioning. In Methods in Membrane Lipids, D.M. Owen, ed. (New York, NY: Springer), pp. 65–77.

Levental, I., Lingwood, D., Grzybek, M., Coskun, U., and Simons, K. (2010). Palmitoylation regulates raft affinity for the majority of integral raft proteins. Proc. Natl. Acad. Sci. U. S. A. *107*, 22050–22054.

Levental, I., Levental, K.R., and Heberle, F.A. (2020a). Lipid Rafts: Controversies Resolved, Mysteries Remain. Trends Cell Biol. *30*, 341–353.

Levental, K.R., Surma, M.A., Skinkle, A.D., Lorent, J.H., Zhou, Y., Klose, C., Chang, J.T., Hancock, J.F., and Levental, I. (2017). ω-3 polyunsaturated fatty acids direct differentiation of the membrane phenotype in mesenchymal stem cells to potentiate osteogenesis. Sci. Adv. *3*, eaao1193.

Levental, K.R., Malmberg, E., Symons, J.L., Fan, Y.-Y., Chapkin, R.S., Ernst, R., and Levental, I. (2020b). Lipidomic and biophysical homeostasis of mammalian membranes counteracts dietary lipid perturbations to maintain cellular fitness. Nat. Commun. *11*, 1339.

Li, G., Wang, Q., Kakuda, S., and London, E. (2020). Nanodomains can persist at physiologic temperature in plasma membrane vesicles and be modulated by altering cell lipids[S]. J. Lipid Res. *61*, 758–766.

Lingwood, D., and Simons, K. (2010). Lipid rafts as a membrane-organizing principle. Science *327*, 46–50.

Liu, A.P., and Fletcher, D.A. (2006). Actin Polymerization Serves as a Membrane Domain Switch in Model Lipid Bilayers. Biophys. J. *91*, 4064–4070.

Lorent, J.H., Diaz-Rohrer, B., Lin, X., Spring, K., Gorfe, A.A., Levental, K.R., and Levental, I. (2017). Structural determinants and functional consequences of protein affinity for membrane rafts. Nat. Commun. *8*, 1219.

Lyon, A.S., Peeples, W.B., and Rosen, M.K. (2021). A framework for understanding the functions of biomolecular condensates across scales. Nat. Rev. Mol. Cell Biol. *22*, 215–235.

Machta, B.B., Papanikolaou, S., Sethna, J.P., and Veatch, S.L. (2011). Minimal Model of Plasma Membrane Heterogeneity Requires Coupling Cortical Actin to Criticality. Biophys. J. *100*, 1668–1677.

Machta, B.B., Veatch, S.L., and Sethna, J.P. (2012). Critical Casimir Forces in Cellular Membranes. Phys. Rev. Lett. *109*, 138101.

Machta, B.B., Gray, E., Nouri, M., McCarthy, N.L.C., Gray, E.M., Miller, A.L., Brooks, N.J., and Veatch, S.L. (2016). Conditions that Stabilize Membrane Domains Also Antagonize n-Alcohol Anesthesia. Biophys. J. *111*, 537–545.

Manley, S., Horton, M.R., Lecszynski, S., and Gast, A.P. (2008). Sorting of Streptavidin Protein Coats on Phase-Separating Model Membranes. Biophys. J. *95*, 2301–2307.

Marshall, A.J., Niiro, H., Yun, T.J., and Clark, E.A. (2000). Regulation of B-cell activation and differentiation by the phosphatidylinositol 3-kinase and phospholipase Cgamma pathway. Immunol. Rev. *176*, 30–46.

Mattila, P.K., Batista, F.D., and Treanor, B. (2016). Dynamics of the actin cytoskeleton mediates receptor cross talk: An emerging concept in tuning receptor signaling. J. Cell Biol. *212*, 267–280.

McKeithan, T.W. (1995). Kinetic proofreading in T-cell receptor signal transduction. Proc. Natl. Acad. Sci. *92*, 5042–5046.

Munro, S. (2003). Lipid Rafts: Elusive or Illusive? Cell *115*, 377–388.

Oldfield, E., and Chapman, D. (1972). Dynamics of lipids in membranes: Heterogeneity and the role of cholesterol. FEBS Lett. *23*, 285–297.

Ovesný, M., Křížek, P., Borkovec, J., Svindrych, Z., and Hagen, G.M. (2014). ThunderSTORM: a comprehensive ImageJ plug-in for PALM and STORM data analysis and super-resolution imaging. Bioinforma. Oxf. Engl. *30*, 2389–2390.

Packard, T.A., and Cambier, J.C. (2013). B lymphocyte antigen receptor signaling: initiation, amplification, and regulation. F1000prime Rep. *5*, 40.

Pathak, P., and London, E. (2015). The Effect of Membrane Lipid Composition on the Formation of Lipid Ultrananodomains. Biophys. J. *109*, 1630–1638.

Pierce, S.K., and Liu, W. (2010). The tipping points in the initiation of B cell signalling: how small changes make big differences. Nat. Rev. Immunol. *10*, 767–777.

Pore, D., and Gupta, N. (2015). Ezrin-Radixin-Moesin family proteins in the regulation of B cell immune response. Crit. Rev. Immunol. *35*, 15–31.

Saffman, P.G., and Delbrück, M. (1975). Brownian motion in biological membranes. Proc. Natl. Acad. Sci. *72*, 3111–3113.

Sanchez, S.A., Tricerri, M.A., and Gratton, E. (2012). Laurdan generalized polarization fluctuations measures membrane packing micro-heterogeneity in vivo. Proc. Natl. Acad. Sci. U. S. A. *109*, 7314–7319.

Schmid, F. (2017). Physical mechanisms of micro- and nanodomain formation in multicomponent lipid membranes. Biochim. Biophys. Acta BBA - Biomembr. *1859*, 509–528.

Schneider, F., Waithe, D., Clausen, M.P., Galiani, S., Koller, T., Ozhan, G., Eggeling, C., and Sezgin, E. (2017). Diffusion of lipids and GPI-anchored proteins in actin-free plasma membrane vesicles measured by STED-FCS. Mol. Biol. Cell *28*, 1507–1518.

Sengupta, P., Holowka, D., and Baird, B. (2007). Fluorescence resonance energy transfer between lipid probes detects nanoscopic heterogeneity in the plasma membrane of live cells. Biophys. J. *92*, 3564–3574.

Sezgin, E., Kaiser, H.-J., Baumgart, T., Schwille, P., Simons, K., and Levental, I. (2012). Elucidating membrane structure and protein behavior using giant plasma membrane vesicles. Nat. Protoc. *7*, 1042–1051.

Shaw, T.R., Ghosh, S., and Veatch, S.L. (2021). Critical Phenomena in Plasma Membrane Organization and Function. Annu. Rev. Phys. Chem. *72*, null.

Shelby, S.A., Veatch, S.L., Holowka, D.A., and Baird, B.A. (2016). Functional nanoscale coupling of Lyn kinase with IgE-FcεRI is restricted by the actin cytoskeleton in early antigen-stimulated signaling. Mol. Biol. Cell *27*, 3645–3658.

Shin, Y., and Brangwynne, C.P. (2017). Liquid phase condensation in cell physiology and disease. Science *357*.

Simons, K., and Ikonen, E. (1997). Functional rafts in cell membranes. Nature *387*, 569–572.

Sohn, H.W., Tolar, P., Jin, T., and Pierce, S.K. (2006). Fluorescence resonance energy transfer in living cells reveals dynamic membrane changes in the initiation of B cell signaling. Proc. Natl. Acad. Sci. U. S. A. *103*, 8143–8148.

Sorre, B., Callan-Jones, A., Manneville, J.-B., Nassoy, P., Joanny, J.-F., Prost, J., Goud, B., and Bassereau, P. (2009). Curvature-driven lipid sorting needs proximity to a demixing point and is aided by proteins. Proc. Natl. Acad. Sci. *106*, 5622–5626.

St. Clair, J.W., Kakuda, S., and London, E. (2020). Induction of Ordered Lipid Raft Domain Formation by Loss of Lipid Asymmetry. Biophys. J. *119*, 483–492.

Stone, M.B., and Veatch, S.L. (2014). Far-Red Organic Fluorophores Contain a Fluorescent Impurity. ChemPhysChem *15*, 2240–2246.

Stone, M.B., and Veatch, S.L. (2015). Steady-state cross-correlations for live two-colour super-resolution localization data sets. Nat. Commun. *6*.

Stone, M.B., Shelby, S.A., Núñez, M.F., Wisser, K., and Veatch, S.L. (2017). Protein sorting by lipid phase-like domains supports emergent signaling function in B lymphocyte plasma membranes. ELife *6*, e19891.

Tischer, D.K., and Weiner, O.D. (2019). Light-based tuning of ligand half-life supports kinetic proofreading model of T cell signaling. ELife *8*, e42498.

Tolar, P., Hanna, J., Krueger, P.D., and Pierce, S.K. (2009). The constant region of the membrane immunoglobulin mediates B cell-receptor clustering and signaling in response to membrane antigens. Immunity *30*, 44–55.

Veatch, S.L., Cicuta, P., Sengupta, P., Honerkamp-Smith, A., Holowka, D., and Baird, B. (2008). Critical Fluctuations in Plasma Membrane Vesicles. ACS Chem. Biol. *3*, 287–293.

Veatch, S.L., Machta, B.B., Shelby, S.A., Chiang, E.N., Holowka, D.A., and Baird, B.A. (2012). Correlation Functions Quantify Super-Resolution Images and Estimate Apparent Clustering Due to Over-Counting. PLoS ONE *7*, e31457.

Vogel, S.K., Greiss, F., Khmelinskaia, A., and Schwille, P. (2017). Control of lipid domain organization by a biomimetic contractile actomyosin cortex. ELife *6*, e24350.

Yousefi, O.S., Günther, M., Hörner, M., Chalupsky, J., Wess, M., Brandl, S.M., Smith, R.W., Fleck, C., Kunkel, T., Zurbriggen, M.D., et al. (2019). Optogenetic control shows that kinetic proofreading regulates the activity of the T cell receptor. ELife *8*, e42475.

Zhao, J., Wu, J., and Veatch, S.L. (2013). Adhesion Stabilizes Robust Lipid Heterogeneity in Supercritical Membranes at Physiological Temperature. Biophys. J. *104*, 825–834.

Zhou, Y., Maxwell, K.N., Sezgin, E., Lu, M., Liang, H., Hancock, J.F., Dial, E.J., Lichtenberger, L.M., and Levental, I. (2013). Bile Acids Modulate Signaling by Functional Perturbation of Plasma Membrane Domains. J. Biol. Chem. *288*, 35660–35670.